Title

A Generalized Pyrolysis Model for Simulating Charring, Intumescent, Smoldering, and Noncharring Gasification

Authors

Lautenberger, Chris
Fernandez-Pello, Carlos

Publication Date

2006-08-27

A Generalized Pyrolysis Model for Simulating Charring, Intumescent, Smoldering, and Noncharring Gasification

Chris Lautenberger and Carlos Fernandez-Pello*

Department of Mechanical Engineering,
University of California, Berkeley
Berkeley, CA 94720, USA.

* *Corresponding author. Tel: 510-642-6554; Fax: 510-642-1850; Email:* ferpello@me.berkeley.edu.

Abstract

This paper presents a generalized pyrolysis model that can simulate the gasification of noncharring, charring, and intumescent materials, as well as smoldering in porous media. Separate conservation equations are solved for gaseous and condensed phase mass and species, solid phase energy, and gas-phase momentum. An arbitrary number of gas-phase and condensed-phase species can be accommodated, each having its own temperature-dependent thermophysical properties. The user may specify any number of solid to gas, solid to solid, or solid + gas to solid + gas reactions of any order. Both in-depth radiation transfer through a semi-transparent medium as well as radiation transport across pores are considered, and melting is modeled using an apparent specific heat. All volatiles generated inside the solid escape to the ambient with no resistance to flow unless the pressure solver is invoked to solve for the pressure distribution in the solid, with the resultant flow of volatiles calculated according to Darcy's law. Similarly, the user may invoke a gas-phase convective-diffusive solver that determines the composition of the volatiles, including diffusion of species from the ambient into the solid. Thus, in addition to calculating the mass-flux of volatiles escaping from the solid, the actual composition of the vapors can be predicted. To aid in determining the required material properties, the pyrolysis model is coupled to a genetic algorithm that can be used to estimate the required input parameters from bench-scale fire tests, thermogravimetric analysis, or a combination thereof. Model predictions are compared to experimental data for the thermo-oxidative decomposition of a non-charring solid (PMMA) and the thermal pyrolysis of a charring solid (white pine), as well as the gasification and swelling of an intumescent coating, and finally smoldering in polyurethane foam. The predictive capabilities of the model are shown to be generally quite good.

Key Words: Pyrolysis modeling

Nomenclature

Letters

A	Pre-exponential factor
c	Specific heat capacity
E	Activation energy
h	Enthalpy
h_c	Convective heat transfer coefficient
k	Thermal conductivity (Eq. 4), or reaction rate (Eq. 29)
k_b	Boltzmann constant
K	Permeability or number of reactions
m	Mass
$\dot{m}''$	Mass flux
M	Molecular weight or number of condensed-phase species
N	Number of gaseous species
n	Exponent (reaction order, O_2 sensitivity, property temperature dependence)
P	Pressure
$\dot{q}''$	Heat flux
$\dot{Q}'''$	Heat generation per unit volume
R	Universal gas constant
t	Time
T	Temperature
X	Volume fraction
y	Yield
Y	Mass fraction
z	Distance
Δz	Grid size

Greek Symbols

α	Conversion or thermal diffusivity
γ	Radiative conductivity parameter, see Eq. 4
δ	Thickness
ζ	Dummy variable of integration
ε	Emissivity or maximum energy of attraction in Chapman Enskog theory
κ	Absorption coefficient
μ	Viscosity
ν	Viscosity (μ/ρ)
ρ	Density
σ	Stefan-Boltzmann constant or collision diameter
σ^2	Variance of latent heat of melting, see Eq. 7
χ	Fraction of density difference realized as gases
ψ	Porosity
$\dot{\omega}'''$	Reaction rate
Ω_D	Function of dimensionless temperature in Eq. 13
Ω_μ	Function of dimensionless temperature in Eq. 12

Subscripts

0	Initial
∞	Ambient or final
A	Species A
b	Baseline
B	Species B
c	Specific heat capacity
e	External
g	Gaseous
i	Condensed phase species i
j	Gaseous species j
k	Thermal conductivity or reaction index
ℓ	Condensed phase species ℓ
m	Melt
p	Pressure
P	Point
r	Radiative (Eq. 4) or reference (Eq. 3)
s	Solid
ρ	Density

Superscripts

$\bar{(\ )}$	Averaged
$^\circ$	Reference state
*	old (Eq. 49) or modified (Eq. 33 - 35)

1. Introduction

One of the most promising long-term goals of fire modeling is the prediction of large-scale fire development. This involves the coupling of a gas-phase model to handle fluid mechanics, heat transfer, and combustion to a condensed-phase "pyrolysis model" that simulates the heating and gasification of condensed-phase fuels. Although pyrolysis modeling has received considerable attention from the fire community (with no fewer than seven reviews having been published since 1993 [1-7]), it is rare for a pyrolysis model to be applied outside of the research environment in which it was developed. This is mainly due to the difficulty associated with determining the model parameters required to characterize practical materials combined with the fact that pyrolysis models have traditionally been formulated in a way that makes them applicable only to a particular class of materials (*e.g.* noncharring [8], charring [9], intumescent [10], or smoldering combustion [11]) thereby limiting their applicability.

The primary contribution of this paper is the formulation of a broadly applicable generalized pyrolysis model. Rather than developing separate model equations for different classes of materials, the model is kept as general as possible. A particular material is simulated by specifying a set of model parameters (thermophysical properties, reaction mechanisms, *etc*.), and a particular experimental configuration is simulated through specification of initial and boundary conditions. The flexibility to invoke (or omit) submodels for various transport phenomena is retained because there may be little consequence to omitting a particular phenomenon from a simulation other than reducing the computational expense and the number of parameters that must be specified to characterize a material.

Separate conservation equations are solved for gaseous and condensed phase mass and species, solid phase energy, and gas-phase momentum. An arbitrary number of gas-phase and condensed-phase species can be accommodated, each having its own temperature-dependent thermophysical properties. The user may specify any number of solid to gas, solid to solid, or solid + gas to solid + gas reactions of any order. Both in-depth radiation transfer through a semi-transparent medium as well as radiation transport across pores are considered, and melting is modeled using an apparent specific heat. All volatiles generated inside the solid escape to the ambient with no resistance to flow unless the pressure solver is invoked to solve for the pressure distribution in the solid, with the resultant flow of volatiles calculated according to Darcy's law. Similarly, the user may invoke a gas-phase convective-diffusive solver that determines the composition of the volatiles, including diffusion of species from the ambient into the solid. Thus, in addition to calculating the mass-flux of volatiles escaping from the solid, the actual composition of the vapors can be predicted.

To aid in determination of the required material properties, the model has been coupled to a previously developed genetic algorithm [12, 13] that can be used to estimate material properties from laboratory tests. This algorithm has been improved from our earlier work so that it can locate an optimal set of model parameters by comparison of the model predictions to experimental fire test data including transient mass loss rate, in-depth thermocouple measurements, and thickness (an important consideration for intumescent materials) as well as thermal analysis (e.g. thermogravimetric) data. The genetic algorithm has also been parallelized using Message Passing Interface (MPI) and has been run simultaneously in parallel on up to 50

networked PCs. A spreadsheet-based "front-end" to the model has been developed so that all of its features, including the genetic algorithm optimization routines, may be accessed through a single spreadsheet. Finally, the model has been integrated with NIST Fire Dynamics Simulator v4.06 [14] so that it may be applied as a boundary condition in 2D and 3D simulations of ignition, flame spread, and fire growth. The coupled use of this pyrolysis model with FDS for calculating flame spread rates in a simplified laboratory experiment is presented elsewhere [15].

After the model formulation is presented and it is "verified" by comparison of its numerical calculations to several analytical solutions, the model predictions are compared with actual experimental data. To demonstrate the flexibility of the present model, including its ability to account for changes in behavior with changes in ambient oxygen concentration, the model predictions are compared to experimental data for the thermo-oxidative decomposition of a noncharring thermoplastic (PMMA) and the anaerobic pyrolysis of a charring material (white pine). Also simulated are the gasification and swelling of an intumescent coating and propagation of a smolder wave in polyurethane foam.

2. Model formulation

As mentioned earlier, most of the pyrolysis models developed to date have simplifications built into their model equations that limit their applicability to a single class of materials (charring, noncharring, etc.). However, since the most general forms of the equations describing conservation of mass, energy, species, and momentum apply universally, it is possible to formulate a generalized pyrolysis model that can be applied to most solid combustibles. The biggest challenge associated with this task is making enough simplifications and approximations that the number of empirical or adjustable parameters is kept manageable without compromising the generality of the model or neglecting relevant physical phenomena. The model formulation presented below represents an attempt to develop a comprehensive general pyrolysis model while limiting the number of required input parameters. An underlying theme is that the user decides how much complexity or detail to include in a simulation. For example, thermophysical properties may be constant or temperature-dependent, decomposition mechanisms can be single-step or multi-step, radiation can be absorbed only at the surface or in-depth, and so on. Rather than "hardcoding" a certain level of complexity or detail into the governing equations, the user selects the appropriate level via the specified input parameters.

2.1 Preliminaries and definitions

Consider a condensed-phase combustible material that may contain as many as M chemically distinct condensed-phase "species". Examples of different species include a pure polymer, fiber reinforcements in a composite, char, and ash. Within the solid, the initial concentrations of each species may be uniform (as in the case of a homogeneous blended composite) or vary spatially (as in the case of laminated composites or wood). As the solid is heated, it may degrade to form N chemically distinct gaseous species. These species include hydrocarbon fragments (generically, pyrolysate), water vapor, carbon monoxide, *etc*. Throughout this work, the index i (and sometimes ℓ) is used to denote condensed-phase species and the index g,j is used to denote gaseous species. Thus, Y_i is the mass of condensed-phase species i divided by the total mass of all condensed-phase species, and $Y_{g,j}$ is the mass of gaseous species j divided by the mass of all

gaseous species. Note that $Y_{g,j}$ is *not* the mass of gaseous species j divided by the mass of all gaseous and condensed-phase species.

Since the condensed phase is composed of M distinct solid species, each having its own thermophysical properties, the effective properties appearing in the conservation equations presented later must be calculated from the local composition, weighted the appropriate mass or volume fraction where the relation between the mass and volume fraction is:

$$X_i = \overline{\rho} \frac{Y_i}{\rho_i} \tag{1}$$

The convention used here is that quantities with an overbar denote averaged quantities, *i.e.* the weighted density is defined as:

$$\overline{\rho} = \sum_{i=1}^{M} X_i \rho_i \tag{2}$$

Other quantities that are weighted by volume fraction include emissivity ($\overline{\varepsilon} = \sum X_i \varepsilon_i$), radiative absorption coefficient ($\overline{\kappa} = \sum X_i \kappa_i$), porosity ($\overline{\psi} = \sum X_i \psi_i$), permeability ($\overline{K} = \sum K_i \psi_i$), and effective thermal conductivity ($\overline{k} = \sum X_i k_i$).

In Equation 2, ρ_i is the bulk density of species i in its pure form and in a vacuum if it is porous. This is different from the definition sometimes used in other pyrolysis models where ρ_i is the mass of species i per unit volume of mixture. The density of each condensed-phase species is assumed to vary with temperature according to the relation:

$$\rho_i(T) = \rho_{0,i} \left(\frac{T}{T_r} \right)^{n_{\rho,i}} \tag{3}$$

where T_r is a reference temperature, usually taken as 300 K.

The thermal conductivity of each condensed-phase species is broken into a solid and a radiative component ($k_{s,i}$ and $k_{r,i}$ respectively). The latter is attributed to radiation heat transfer across pores and may become a dominant mode of heat transfer in high temperature chars. The effective thermal conductivity of species i is:

$$k_i(T) = k_{s,i}(T) + k_{r,i}(T) = k_{0,i} \left(\frac{T}{T_r} \right)^{n_{k,i}} + \gamma_i \sigma T^3 \tag{4}$$

where γ has units of length and depends on the pore structure (see *e.g.* Lautenberger and Fernandez-Pello [7] for details).

The temperature-dependent specific heat of species i is the sum of the "baseline" specific heat ($c_{b,i}$) and the apparent increase in the specific heat due to the latent heat of melting ($c_{m,i}$):

$$c_i(T) = c_{b,i}(T) + c_{m,i}(T) \tag{5}$$

$$c_{b,i}(T) = c_{0,i}\left(\frac{T}{T_r}\right)^{n_{c,i}} \tag{6}$$

For polymers that melt, the latent heat of melting is assumed to be distributed via a Gaussian peak centered at T_m, the melting temperature:

$$c_{m,i}(T) = \frac{\Delta H_{m,i}}{\sqrt{2\pi\sigma_{m,i}^2}} \exp\left(-\frac{(T - T_{m,i})^2}{2\sigma_{m,i}^2}\right) \tag{7}$$

The assumption in Equation 7 that a species does not have a well-defined melting point is not necessarily a shortcoming of the model because only crystalline solids have a well-defined melting temperature. Most polymers are a mixture of crystalline and amorphous components so that melting (or softening of the amorphous components) usually occurs over a finite temperature range.

The sensible enthalpy of species i at temperature T is determined by integration:

$$\begin{aligned} h_i(T) &= \int_{T^\circ}^{T} \left(c_{b,i}(\theta) + c_{m,i}(\theta)\right) d\theta \\ &= \frac{c_{0,i}}{n_{c,i}+1}\left(T\left(\frac{T}{T_r}\right)^{n_{c,i}} - T^\circ\left(\frac{T^\circ}{T_r}\right)^{n_{c,i}}\right) + \frac{\Delta H_{m,i}}{2}\left(\operatorname{erf}\left(\frac{T - T_{m,i}}{\sqrt{2\sigma_{m,i}^2}}\right) - \operatorname{erf}\left(\frac{T^\circ - T_{m,i}}{\sqrt{2\sigma_{m,i}^2}}\right)\right) \end{aligned} \tag{8}$$

The averaged enthalpy and specific heat are determined as mass-weighted quantities, i.e. $\overline{c} = \sum_{i=1}^{M} Y_i c_i$ and $\overline{h} = \sum_{i=1}^{M} h_i Y_i$. In addition to the above condensed-phase properties, definitions of several gas-phase quantities are necessary. The gas-phase density is calculated from the ideal gas law:

$$\overline{\rho}_g = \frac{P\overline{M}_g}{RT_g} \tag{9}$$

Where $\overline{M}_g$ is calculated from the local volume fractions of all gaseous species. The specific heat of gaseous species j is assumed to be of the form:

$$c_{p,j}(T) = a_{0,j} + a_{1,j}T + a_{2,j}T^2 + a_{3,j}T^4 \tag{10}$$

Therefore, the sensible enthalpy of gaseous species *j* is:

$$\begin{aligned} h_{g,j}(T) &= \int_{T^\circ}^{T} c_{pg,j}(\tau)d\tau \\ &= a_{0,j}\left(T - T^\circ\right) + \frac{1}{2}a_{1,j}\left(T^2 - T^{\circ 2}\right) + \frac{1}{3}a_{2,j}\left(T^3 - T^{\circ 3}\right) + \frac{1}{4}a_{3,j}\left(T^4 - T^{\circ 4}\right) \end{aligned} \tag{11}$$

The average gas-phase sensible enthalpy is weighted by mass, i.e. $\overline{h}_g = \sum_{j=1}^{N} Y_{g,j}h_{g,j}$.

The viscosity μ_j of gaseous species *j* is estimated from Chapman-Enskog theory [16]:

$$\mu_j = 2.6693\times10^{-6}\frac{\sqrt{M_j T}}{\sigma_j^2\Omega_\mu} \tag{12}$$

where σ_j is the collision diameter of species *j* (Å) and Ω_μ is a function of the dimensionless temperature, which is normalized by $(\varepsilon/k_b)_j$ [16] where k_b is the Boltzmann constant and ε is the maximum energy of attraction between a pair of molecules. Thus, σ_j and $(\varepsilon/k_b)_j$ are model parameters that describe the viscosity of gaseous species *j*. They are tabulated for several gases (along with the function $\Omega_\mu\left(T/\left(\varepsilon/k_b\right)\right)$) by Bird *et al.* [16]. For simplicity, in this work, the overall viscosity of the mixture is calculated as the mass-weighted sum of the viscosities of the individual components. The greater accuracy that can be obtained sing the formulas in Bird *et al.* [16] to calculate the overall viscosity of multicomponent mixtures does not seem justified given our lack of knowledge regarding the chemical composition of volatiles in decomposing solids. As will be discussed later, the kinematic viscosity ($\nu = \mu/\rho$) is used in the implementation of Darcy's law. It is obtained by dividing the weighted viscosity $\overline{\mu}$ by $\overline{\rho}_g$.

The diffusion coefficients that are used in the gaseous species conservation equation are also calculated from Chapman-Enskog theory. The binary diffusion coefficient for species *A* diffusing into species *B* is:

$$D_{AB} = 0.018829\frac{\sqrt{T^3\left(\frac{1}{M_A}+\frac{1}{M_B}\right)}}{P\sigma_{AB}^2\Omega_{D,AB}} \tag{13a}$$

where $\Omega_{D,AB}$ is a function of $T/\left(\varepsilon_{AB}/k_b\right)$ tabulated by Bird et al. [16], and the parameters σ_{AB} and ε_{AB} are weighted averages between molecules *A* and *B*:

$$\sigma_{AB} = \frac{1}{2}\left(\sigma_A + \sigma_B\right) \tag{13b}$$

$$\varepsilon_{AB} = \sqrt{\varepsilon_A \varepsilon_B} \tag{13b}$$

In the model, all species are assigned the same diffusivity, taken as that of oxygen into the primary pyrolysate species, usually species 1. This approximation is justified because very little is known about the composition of the gaseous volatiles.

Note from the above that temperature-dependent condensed-phase properties are incorporated in a simplified way because the functional form of the temperature dependency for k, ρ, and c is assumed *a priori*. Thus, the model can accommodate general trends such as an increase in c with temperature. However, detailed temperature dependencies of the underlying thermophysical properties cannot be included. This is not necessarily a drawback because very rarely are accurate detailed measurements of $k(T)$, $c(T)$, or $\rho(T)$ available, particularly at temperatures above 300 ºC that are most relevant to mass burning. Additionally very few detailed property measurements are available for "intermediate" species such as char or ash. It was felt that the simplicity of a two-parameter model (which was found to work quite well with genetic algorithm optimization) for thermophysical properties outweighs any potential drawbacks associated with the inability to specify detailed temperature dependent properties.

The generality of this formulation should also be noted. For example, if a condensed-phase species that has a constant specific heat and doesn't melt is desired, then the user simply sets $n_{c,i} = 0$ and $\Delta H_{m,i} = 0$. Similarly, radiative transport across pores in a char layer can be simulated by specifying a nonzero value of γ_i (Equation 4), but radiative transport can be eliminated simply by setting $\gamma_i = 0$.

2.2 Condensed-phase mass and species conservation

A key aspect of this model is that it is specifically designed to accommodate volume change, either due to material consumption (surface regression) or swelling (attributed to a solid density that decreases with temperature or intumescence). This is accomplished by assuming that each grid cell (having height Δz) is permeable to gaseous mass transfer but is impermeable to condensed phase mass transfer. Thus, if the condensed-phase density remains constant but gases escape (*e.g.* due to pyrolysis) then Δz decreases to conserve mass. The same occurs if no gases escape but the density increases. Conversely, Δz must increase if the density decreases while no gases escape. Due to this formulation, the grid spacing Δz appears in the conservation of condensed-phase mass and species conservation equations. The continuous form of the condensed-phase mass conservation equation is:

$$\frac{\partial}{\partial t}\left(\overline{\rho}\Delta z\right) + \sum_{j=1}^{N} \dot{\omega}'''_{j,net}\Delta z = 0 \tag{14}$$

where $\dot{\omega}'''_{j,net}$ is the net (production minus destruction) formation rate of gaseous species *j*, and will be described in greater detail later. The condensed-phase species conservation equation is:

$$\frac{\partial}{\partial t}\left(\overline{\rho}\Delta z Y_i\right) = \dot{\omega}'''_{i,net}\Delta z \tag{15}$$

It may seem unusual to see the grid spacing Δz in a conservation equation. However these equations are well-posed because Equations 14 and 15 represent $M + 1$ unknowns in $M + 1$ equations for each grid cell. Specifically, each of the M values of $\overline{\rho}\Delta z Y_i$ are determined from Equation 15, and Equation 14 is solved for $\overline{\rho}\Delta z$. Then, each Y_i is obtained by dividing $\overline{\rho}\Delta z Y_i$ by $\overline{\rho}\Delta z$. The averaged density is then calculated from the relation:

$$\overline{\rho} = \left(\sum_{i=1}^{M}\left(Y_i / \rho_i\right)\right)^{-1} \tag{16}$$

which is obtained summing both sides of Equation 1 over M and solving for $\overline{\rho}$. With $\overline{\rho}$ known, Δz can be determined by dividing $\overline{\rho}\Delta z$ by $\overline{\rho}$. Thus, it can be seen how Y_i, $\overline{\rho}$, and Δz are independently determined from solution of Equations 14 and 15.

2.3 Gas-phase mass and species conservation

The gas-phase conservation of mass equation is:

$$\frac{\partial}{\partial t}\left(\overline{\rho}_g\overline{\psi}\right) + \frac{\partial \dot{m}''_g}{\partial z} = \sum_{j=1}^{N}\dot{\omega}'''_{j,net} - \frac{\overline{\rho}_g\overline{\psi}}{\Delta z}\frac{\partial \Delta z}{\partial t} \tag{17}$$

The last term on the RHS is due to grid stretch. Since it may seem unusual for the grid-spacing to appear in a conservation equation, an alternate but equivalent form of Equation 17 is obtained by substituting the equation for conservation of condensed-phase mass:

$$\frac{\partial}{\partial t}\left(\overline{\rho}_g\overline{\psi}\right) + \frac{\partial \dot{m}''_g}{\partial z} = \sum_{j=1}^{N}\dot{\omega}'''_{j,net} + \frac{\overline{\rho}_g\overline{\psi}}{\overline{\rho}}\left(\frac{\partial \overline{\rho}}{\partial t} + \sum_{j=1}^{N}\dot{\omega}'''_{j,net}\right) \tag{18}$$

Equation 17 is used to obtain the following form of the conservation of gaseous species equation:

$$\overline{\rho}_g\overline{\psi}\frac{\partial Y_{g,j}}{\partial t} + \dot{m}''_g\frac{\partial Y_{g,j}}{\partial z} = \frac{\partial}{\partial z}\left(\overline{\rho}_g D\overline{\psi}\frac{\partial Y_{g,j}}{\partial z}\right) + \dot{\omega}'''_{j,net} - Y_{g,j}\sum_{j=1}^{N}\dot{\omega}'''_{j,net} \tag{19}$$

As described earlier, the diffusion coefficient D is temperature dependent (obtained from Chapman-Enskog theory) is assumed to be identical for all gaseous species and taken as the

binary diffusion coefficient for molecular oxygen into the primary pyrolysate. Eq. 19 is solved with a tridiagonal matrix solver.

2.4 Gas-phase momentum conservation

By assuming that the all gaseous species escape from the condensed phase instantaneously with no resistance, the pyrolysate flux can be obtained (at a fixed time) by integrating Equation 18 in z, *i.e.*:

$$\dot{m}_g''(z) = -\int_{\delta}^{z}\left(\sum_{j=1}^{N}\dot{\omega}_{j,net}''' - \frac{\partial}{\partial t}\left(\overline{\rho}_g\overline{\psi}\right) + \frac{\overline{\rho}_g\overline{\psi}}{\overline{\rho}}\left(\frac{\partial\overline{\rho}}{\partial t} + \sum_{j=1}^{N}\dot{\omega}_{j,net}'''\right)\right)d\zeta \tag{20}$$

Here, the leading negative sign is because the mass flux is defined as positive when flowing into the solid, *i.e.* in the $+z$ direction. The mass flux calculated via Equation 20 is usually "source driven" meaning that the flow is driven by the first term on the RHS which is attributed to generation of gaseous volatiles. However, one can envision a situation in which there is no generation of gaseous volatiles and the condensed-phase density is constant, yet the mass flux calculated with Equation 20 is nonzero: consider a porous medium that is heated, causing a decrease in gas-phase density. A nonzero mass flux results due to the second term on the RHS of Equation 20.

In lieu of using Equation 20 to calculate the mass flux, the user has the option of invoking a pressure solver to calculate the pressure distribution within the solid. Then, the mass flux is calculated according to the pressure gradient according to Darcy's law:

$$\dot{m}_g'' = -\frac{\overline{K}}{\overline{\nu}}\frac{\partial P}{\partial z} \tag{21}$$

An equation for the pressure evolution is obtained by substituting Equation 21 into Equation 17 and introducing the ideal gas law:

$$\frac{\psi\overline{M}_g}{RT_g}\frac{\partial P}{\partial t} = \frac{\partial}{\partial z}\left(\frac{\overline{K}}{\overline{\nu}}\frac{\partial P}{\partial z}\right) + \sum_{j=1}^{N}\dot{\omega}_{j,net}''' + \overline{\rho}_g\overline{\psi}\left(\frac{1}{T_g}\frac{\partial T_g}{\partial t} - \frac{1}{\overline{M}_g}\frac{\partial\overline{M}_g}{\partial t} - \frac{1}{\overline{\psi}}\frac{\partial\overline{\psi}}{\partial t} - \frac{1}{\Delta z}\frac{\partial\Delta z}{\partial t}\right) \tag{22}$$

Note that Equation 22 is similar in form to the heat conduction equation. It is solved with a tridiagonal matrix solver, treating the entire RHS as a source term.

2.5 Energy conservation

The condensed-phase energy conservation equation is formulated in terms of enthalpy, defined for species i in Eq. 8. It can be written as:

$$\frac{\partial\left(\overline{\rho}\overline{h}\right)}{\partial t}+\frac{\partial}{\partial z}\left(\dot{m}''\overline{h}_g\right)=\frac{\partial}{\partial z}\left(\frac{\overline{k}}{\overline{c}}\frac{\partial\overline{h}}{\partial z}\right)+\frac{\partial\dot{q}_r''}{\partial z}+\dot{Q}'''-\frac{\overline{\rho}\overline{h}}{\Delta z}\frac{\partial\Delta z}{\partial t} \tag{23}$$

Changes in kinetic energy, potential energy, and work done by the system on the surroundings have been neglected. The last term on the RHS is due to swelling or contraction. Equation 29 can be simplified by introducing the condensed-phase continuity equation (Equation 14):

$$\overline{\rho}\frac{\partial\overline{h}}{\partial t}+\frac{\partial}{\partial z}\left(\dot{m}''\overline{h}_g\right)=\frac{\partial}{\partial z}\left(\frac{\overline{k}}{\overline{c}}\frac{\partial\overline{h}}{\partial z}\right)+\frac{\partial\dot{q}_r''}{\partial z}+\dot{Q}'''-\overline{\rho}\overline{h}\sum_{j=1}^{N}\dot{\omega}_{j,net}''' \tag{24}$$

Equation 24 is solved with a tridiagonal matrix solver. Note that the in-depth radiative heat flux is:

$$\dot{q}_r''(z)=-\overline{\varepsilon}\dot{q}_e''\exp\left(-\int_0^z\overline{\kappa}(\zeta)d\zeta\right) \tag{25}$$

and its divergence (appearing in Equation 24) is:

$$\frac{\partial\dot{q}_r''}{\partial z}=\overline{\varepsilon}\dot{q}_e''\overline{\kappa}(z)\exp\left(-\int_0^z\overline{\kappa}(\zeta)d\zeta\right) \tag{26}$$

Note the if $\overline{\kappa}$ is not a function of z, then $\partial\dot{q}_r''/\partial z=\overline{\varepsilon}\dot{q}_e''\overline{\kappa}\exp(-\overline{\kappa}z)$.

The gas-phase energy equation is not solved. Rather, thermal equilibrium between the gaseous and condensed phases is assumed, and the gas-phase energy equation simplifies to:

$$T_g=T \tag{27}$$

This approximation is justified because the volumetric heat capacity of the solid-phase is at least one order of magnitude greater than that of the gas-phase. It should be noted that although the gas-phase energy equation is not explicitly solved, there is still heat transfer between the gaseous and condensed phases, *i.e.* the second term on the LHS of Equation 24.

2.6 Initial and boundary conditions

The initial temperature, pressure, gaseous species mass fractions, and condensed-phase species mass fractions are specified by the user. The model assumes that all quantities are initially uniform throughout the thickness of the solid, with the exception of the condensed-phase species mass fractions. The user specifies a number of "layers" and the associated mass fraction of each condensed-phase species in each layer to simulate layered or laminated structure. For a homogeneous solid, there is only a single layer.

The boundary condition for the energy equation at the front face (z = 0) is a balance between incoming thermal radiation and heat losses by radiant emission and Newtonian cooling. If $\overline{\kappa}\big|_{z=0} \neq \infty$ then no radiation is absorbed at the surface because it is absorbed volumetrically in-depth (Equation 26). The back-face boundary condition is either Newtonian cooling to the ambient, or heat loss across a gap (characterized by a user-specified contact resistance) to an underlying inert substrate (*e.g.* calcium silicate) with user-specified thermal properties and thickness. The boundary condition at the back face of the substrate is Newtonian cooling to the ambient.

No boundary conditions are required for the condensed-phase species conservation equation because the model assumes that no condensed-phase mass crosses a cell. The boundary conditions on the pressure evolution equation are such that the pressure gradient at the back face is set to give the user-specified mass flux rate into the back of the solid (usually zero for an impermeable substrate, but nonzero *e.g.* for simulation of smoldering combustion with an internal forced flow). The pressure at the front-face is set to the ambient value.

For the gas-phase convective-diffusive solver, the appropriate species mass fractions entering the back face are set so that the mass flux rate of each gaseous species into the solid is fixed. Normally, the back face is impermeable so there is no flow of volatiles across the back face (the main exception is smoldering combustion with an internal forced flow). As explained by Patankar [17], no boundary condition is required for gaseous species at the front face, unless they are diffusing from the ambient into the solid. If this is the case, then the mass flux rate of a species diffusing into the solid is estimated as $\dot{m}''_j = h_c\left(\overline{\psi}/c_{p,g}\right)\big|_{z=0}\left(Y_{j,\infty} - Y_j\big|_{z=0}\right)$. When the model is coupled to a CFD code, the flux of a gaseous species into the condensed-phase would be calculated from the gradient of the species mass fraction, just as convective heat transfer is calculated from a gas-phase temperature gradient.

3.0 Reaction rates and source terms

The conservation equations that are solved by the model are presented above, but they contain several source terms that must be evaluated. Consider a thermogravimetric (TG) experiment. For a sample with initial mass m_0, the conversion α is defined as:

$$\alpha = \frac{m_0 - m}{m_0 - m_\infty} \tag{28}$$

where m_∞ is the sample mass at the end of the experiment. For materials that leave no residue (such as noncharring polymers), m_∞ = 0 and therefore $\alpha = 1 - m/m_0$. TG data are usually analyzed within the framework of a kinetic model of the form:

$$\frac{\mathrm{d}\alpha}{\mathrm{d}t} = k(T) f(\alpha) \tag{29}$$

In Eq. 29, $k(T)$ is a function carrying the temperature-dependency of the reaction rate and $f(a)$ is the "reaction model", usually assumed to be:

$$f(\alpha) = (1-\alpha)^n \tag{30}$$

where n is the reaction order. Note that for a noncharring polymer $1 - \alpha = m/m_0$. With few exceptions, the function $k(T)$ is assumed to take an Arrhenius form:

$$k(T) = A\exp\left(-\frac{E}{RT}\right) \tag{31}$$

where A is the frequency factor (or pre-exponential factor) and E is the activation energy. After combining Eqs. 29-31, the time rate of change of α becomes:

$$\frac{\mathrm{d}\alpha}{\mathrm{d}t} = A\exp\left(-\frac{E}{RT}\right)(1-\alpha)^n \tag{32}$$

Eqs. 29 - 32 are the starting point for the treatment of solid-phase reactions in this model. First, define $1 - \alpha_i$ as:

$$1-\alpha_i = \frac{m_i''}{m_{0i}''^*} = \frac{\overline{\rho} Y_i \Delta z}{(\overline{\rho} Y_i \Delta z)_0^*} \tag{33}$$

where $(\overline{\rho} Y_i \Delta z)_0^*$ is defined as follows:

$$(\overline{\rho} Y_i \Delta z)_0^* = (\overline{\rho} Y_i \Delta z)\big|_{t=0} + \int_0^t \dot{\omega}_{fi}'''(\tau)\Delta z(\tau) d\tau \tag{34}$$

Here $\dot{\omega}_{fi}'''$ is the formation rate of species i (not the net formation rate or formation minus destruction). Each reaction is classified as either thermal pyrolysis or thermooxidative decomposition, with the reaction rates calculated respectively as:

$$\dot{\omega}_{di,k}''' = \left(\frac{\overline{\rho} Y_i \Delta z}{(\overline{\rho} Y_i \Delta z)_0^*}\right)^{n_k} \frac{(\overline{\rho} Y_i \Delta z)_0^*}{\Delta z} A_k \exp\left(-\frac{E_k}{RT}\right) \quad (\text{for } n_{O_2,k} = 0) \tag{35a}$$

$$\dot{\omega}_{di,k}''' = \left(\frac{\overline{\rho} Y_i \Delta z}{(\overline{\rho} Y_i \Delta z)_0^*}\right)^{n_k} \frac{(\overline{\rho} Y_i \Delta z)_0^*}{\Delta z} \left[(1+Y_{O_2})^{n_{O_2,k}} - 1\right] A_k \exp\left(-\frac{E_k}{RT}\right) \quad (\text{for } n_{O_2,k} \neq 0) \tag{35b}$$

Thus, each reaction is characterized by four parameters: 1) n_k (reaction order in remaining solid), 2) $n_{O_2,k}$ (reaction order in gaseous oxygen mass fraction), 3) A_k (pre-exponential factor), and 4) E_k (activation energy). In Equation 35, the oxygen mass fraction (Y_{O_2}) is the local value in the condensed phase, as determined by solution of Eq. 19, and not the freestream value. The exponent $n_{O_2,k}$ describes the oxygen sensitivity of reaction *k,* and a value of $n_{O_2,k} = 0$ is specified for reactions that do not involve oxygen. Note that for the special case of $n_k = 1$ and $n_{O_2,k} = 0$, Equation 35 reduces to the following familiar form:

$$\dot{\omega}'''_{di,k} = \overline{\rho} Y_i A_k \exp\left(-\frac{E_k}{RT}\right) \tag{36}$$

To simplify the treatment of the solid-solid reactions, each reaction transforms species *i* into no more than one additional condensed-phase species. However, the user may specify multiple reactions that transform species *i* to different species, with the net effect that species *i* can actually be transformed into multiple species. Assume here that reaction *k* transforms condensed phase species *i* to condensed phase species ℓ plus gases (the composition of the gases will be specified later). Then, the formation rate of species ℓ from species *i* due to reaction *k* is:

$$\dot{\omega}'''_{f\ell,i,k} = \left[1 + \left(\frac{\rho_\ell}{\rho_i} - 1\right)\chi_k\right]\dot{\omega}'''_{di,k} \tag{37}$$

And the formation rate of gases due to consumption of species *i* by reaction *k* is:

$$\dot{\omega}'''_{fg,i,k} = \left[\left(1 - \frac{\rho_\ell}{\rho_i}\right)\chi_k\right]\dot{\omega}'''_{di,k} \tag{38}$$

In Equations 37 and 38, the parameter χ_k is the fraction of the density difference between species *i* and ℓ that is realized as gases. For a noncharring reaction, no residue remains and the reaction completely transforms the condensed phase species *i* to gases, so we set $\rho_\ell = 0$ and $\chi_k = 1$. Then, the quantity in square brackets in Equation 37 becomes zero so the formation rate of condensed-phase species ℓ is also zero. At the same time, the quantity in square brackets in Equation 38 becomes 1, meaning that only gases are generated from the reaction.

Equations 37 and 38 can also be used to model a charring reaction. If $\chi_k = 1$ and $0 < \rho_\ell < \rho_i$, it can be seen that the formation rate of condensed-phase species *i* and gaseous species *j* are both nonzero. This is very similar to the traditional approach to modeling the pyrolysis of charring materials.

Finally, Equations 37 and 38 can be used to model an intumescent material by setting $0 \le \chi_k < 1$. Then, provided $\rho_\ell < \rho_i$, a lower density solid is formed from a higher density solid and swelling

occurs to conserve mass because the decrease in $\overline{\rho}$ compensated for by an increase in Δz through Equation 14. In the extreme case of $\chi_k = 0$, the material swells without any escape of gases. Values of χ_k between 0 and 1 are permitted, causing intumescence (swelling) to occur simultaneously with the release of gaseous vapors. The amount of swelling compared to the amount of volatilization is dictated by the value of χ_k. This is how intumescent materials actually work because blowing agents form a low density porous char with an accompanying release of gases.

Note that adding Equations 37 and 38 gives:

$$\dot{\omega}'''_{f\ell,i,k} + \dot{\omega}'''_{fg,i,k} = \dot{\omega}'''_{di,k} \tag{39}$$

In words, the formation rate of condensed-phase species ℓ by reaction k plus the formation rate of gases by reaction k equals the destruction rate of condensed-phase species i by reaction k.

The total destruction rate of condensed-phase species i and the total formation rate of condensed-phase species ℓ are obtained by summing over all reactions:

$$\dot{\omega}'''_{di} = \sum_{k=1}^{K} \dot{\omega}'''_{di,k} \tag{40}$$

$$\dot{\omega}'''_{f\ell} = \sum_{k=1}^{K} \dot{\omega}'''_{f\ell,i,k} \tag{41}$$

Then, the net creation rate of a condensed-phase species (*i.e.* the source term in Equation 15) is obtained by difference:

$$\dot{\omega}'''_{i,net} = \dot{\omega}'''_{fi} - \dot{\omega}'''_{di} \tag{42}$$

The preceding discussion explains how the net source terms for the condensed-phase species conservation equations are calculated. However, the net source terms for the gaseous species conservation equations are still needed. Recall that Equation 38 gives the formation rate of gases due to reaction k. However, it does not contain any information regarding the composition of the gases that are generated. This is specified here by a "species yield matrix" that describes the distribution of the gaseous species formed by each reaction, *i.e.* the generation rate of gaseous species j from reaction k is calculated as:

$$\dot{\omega}'''_{j,k} = \dot{\omega}'''_{fg,i,k} y_{j,k} \tag{43}$$

where $y_{j,k}$ is the N by K "species yield matrix". Its entries may be positive or negative, with a positive value corresponding to production of a gaseous species, and a negative value corresponding to consumption of a gaseous species. Normally, oxygen is the only species that

has a negative yield (because it is consumed in, for example, char oxidation). Note that in order to conserve mass, the sum of all nonzero entries in any column of the species yield matrix must add to unity. The net formation rate of species j (appearing in Equation 19) is obtained by summing over all reactions:

$$\dot{\omega}'''_{j,net} = \sum_{k=1}^{K} \dot{\omega}'''_{j,k} y_{j,k} \tag{44}$$

Note that the source terms for the gaseous species equations do not include gas-gas reactions, *e.g.* the reaction of pyrolysate with oxygen to form combustion products and release heat. This may be an important consideration for pyrolysate moving through a high temperature char layer where oxygen is present as well as modeling the autoignition of solids and the transition from smoldering to flaming combustion in porous media. Since the gas-phase conservation equation can accommodate gas-gas reactions, this may be added to the model in the future.

The heat of reaction associated with the formation of each gaseous species j by reaction k is calculated by an N by K "enthalpy of reaction matrix" just as the formation rate of each gaseous species j by reaction k is specified by the yield matrix. That is, the heat of reaction due to the formation of gaseous species j by reaction k is:

$$\dot{Q}'''_{j,k} = \dot{\omega}'''_{j,k} \Delta H_{j,k} \tag{45}$$

As with the species yield matrix, the enthalpy of reaction matrix may contain either positive or negative entries. Whether a positive or negative entry in the enthalpy of reaction matrix represents an endothermic or exothermic reaction depends on whether a species is created or consumed (*i.e.* whether it has a positive or negative entry in the species yield matrix). Summing Equation 45 over all gaseous species j and all reactions k gives the heat source/sink due to gaseous reactions:

$$\dot{Q}'''_{g} = \sum_{k=1}^{K} \sum_{j=1}^{N} \dot{\omega}'''_{j,k} \Delta H_{j,k} \tag{46}$$

There are also source terms that must be considered in the energy equation that are attributed to condensed-phase reactions, *i.e.* due to reaction k moving the enthalpy of condensed-phase phase species i to the gas phase and the change in enthalpy when species i is converted to species ℓ:

$$\dot{Q}'''_{s} = \sum_{k=1}^{K} \left(\dot{\omega}'''_{f\ell,i,k} \left(h_i - h_\ell \right) - \dot{\omega}'''_{f\ell,i,k} \Delta H_{i,\ell} - \dot{\omega}'''_{fg,i,k} h_i \right) \tag{47}$$

The first term on the RHS of Equation 47 accounts for the change in sensible enthalpy when species ℓ is formed from the parent species i and the enthalpy of species ℓ is not the same as that of species i. If the enthalpy of species ℓ is greater than that of species i, then heat must be absorbed to produce species ℓ so the reaction is endothermic. Conversely, if the enthalpy of

species ℓ is less than that of species i, then heat is released when species ℓ is produced so the reaction is exothermic. The second term on the RHS Equation 47 is attributed to the difference in chemical or latent enthalpy between condensed-phase species i and ℓ. When it is positive, an endothermic reaction occurs and when it is negative an exothermic reaction occurs. Finally, the last term on the RHS Equation 47 represents the enthalpy transfer from the condensed phase to the gas-phase when species i is gasified. The source term appearing in the energy equation is the sum of Equations 46 and 47:

$$\dot{Q}''' = \dot{Q}'''_g + \dot{Q}'''_s \tag{48}$$

4. Solution methodology

The governing equations presented above describe conservation of gaseous and condensed-phase mass and species, gas-phase momentum, and solid-phase energy (*i.e.* Equations 14, 15, 19, 22, and, 24). These continuous differential equations are discretized (following closely the recommendations of Patankar [17]) to yield a system of coupled algebraic equations. The "stencil" used for this discretization is shown in Figure 1. Cell P ("point") has neighboring cells T ("top") and B ("bottom"). The interface between cell P and T is denoted t, and similarly the interface between cell P and B is denoted b. It is assumed that the value at the center of a particular cell prevails over the entire cell. The notation ϕ_T indicates the value of variable ϕ in cell T and ϕ_t indicates the value of variable ϕ at the interface between P and T. $(\delta z)_t$ is the distance from point P to point T and $(\delta z)_b$ is the distance from point P to point B. The height of cell P is $(\Delta z)_P$. Also, note that ϕ^* denotes the value of ϕ at time t and ϕ denotes the value of ϕ at time $t + \Delta t$. For example, the discretized energy equation (with no in-depth radiation absorption for simplicity) can be written as:

$$\overline{\rho}_P \frac{\overline{h}_P - \overline{h}_P^*}{\Delta t} + \frac{\left(\dot{m}''\overline{h}_g\right)_b - \left(\dot{m}''\overline{h}_g\right)_t}{(\Delta z)_P} = \left(\frac{\overline{k}}{\overline{c}}\right)_t \frac{\overline{h}_T - \overline{h}_P}{(\delta z)_t (\Delta z)_P} - \left(\frac{\overline{k}}{\overline{c}}\right)_b \frac{\overline{h}_P - \overline{h}_B}{(\delta z)_b (\Delta z)_P} + \dot{Q}'''_P - \overline{\rho}_P \overline{h}_P \sum_{j=1}^{N} \left(\dot{\omega}'''_{j,net}\right)_P \tag{49}$$

The other equations are discretized in a similar manner. Due to nonlinearity, a fully-implicit formulation is adopted for solution all equations. As described earlier, the discretized conservation of condensed-phase mass and species equations reduce to $M + 1$ coupled ordinary differential equations for each grid point. The user has the option of integrating the ODE's using the stiff solver DVODE or a custom fully implicit solver that uses overrelaxation to prevent divergence between iterations and automatically adjusts the timestep should divergence occur. In the custom solver, the source terms are split into positive and negative components to ensure physically realistic results and prevent negative mass fractions or densities from occurring (see Patankar [17] pg 145).

The remaining equations (gas-phase species, gas-phase momentum, and condensed-phase energy) are solved using a computationally efficient tridiagonal matrix algorithm solver. As with the condensed-phase species equations, source terms for the gas-phase species equation are again split into positive and negative components to ensure all mass fractions remain positive during

iterations. Diffusion coefficients (*e.g.* $\bar{k}/\bar{c}$ in Equation 24) are evaluated as the harmonic mean of cell *P* and its neighbor (*T* or *B*) rather than the arithmetic mean as suggested by Patankar [17].

At the end of a timestep or iteration, the mass-weighted enthalpy ($\bar{h} = \Sigma h_i Y_i$) is known. However, the temperature must be extracted from this mass weighted enthalpy, and Newton's method is used to do this by solving the following equation for the unknown temperature *T* (where $\bar{h}$ and the Y_i's are known):

$$\sum_{i=1}^{M} Y_i h_i(T) = \bar{h} \tag{50}$$

For the special case of all species having constant (temperature invariant) specific heat (*i.e.* $n_{c,i} = 0 \ \forall \, i$) Newton iteration is not required as the temperature can be obtained directly as:

$$T - T^\circ = \frac{\bar{h}}{\sum_{i=1}^{M} Y_i c_{0,i}} \tag{51}$$

To prevent numerical problems that occur as $\Delta z \to 0$ (as occurs when a slab of a noncharring polymer burns completely away), if a cell's thickness decreases below 0.1 Å (0.01 nm) then all reaction rates in that cell are set to zero and that cell behaves as if it was inert. This distance is less than one tenth of the diameter of a single atom and the temperature drop across such a small distance is very small, perhaps 10^{-5} K, so this approximation is considered reasonable.

5. Model verification

In this section the numerical calculations of the model are compared to several analytical solutions to verify that the governing equations described above have correctly been implemented. In addition to this exercise, overall balances for mass, energy, and species conservation have been verified for several different scenarios.

5.1. Semi-infinite solid exposed to constant incident heat flux with surface heat losses by convection only.

Consider a constant property inert homogeneous semi-infinite solid initially at temperature T_0. It is exposed to a constant radiative heat flux at $z = 0$. The solid is perfectly opaque so radiation is absorbed immediately at the surface. The solid loses heat by convection to the ambient at temperature T_0. This problem can be stated mathematically as:

$$\frac{1}{\alpha}\frac{\partial T(z,t)}{\partial t} = \frac{\partial^2 T(z,t)}{\partial z^2} \quad \text{for } 0 \le z < \infty \tag{52a}$$

$$T\big|_{z\to\infty} = T_0 \tag{52b}$$

$$-k\frac{\partial T}{\partial z}\bigg|_{z=0} = -h\big(T - T_0\big)\big|_{z=0} \tag{52c}$$

$$T\big|_{t=0} = T_0 \tag{52d}$$

The solution to this problem is well-known:

$$\frac{T - T_0}{\dot{q}_e''/h} = \operatorname{erfc}\left(\frac{z}{\sqrt{4\alpha t}}\right) - \exp\left(\frac{z}{k/h} + \frac{t}{k\rho c/h^2}\right)\operatorname{erfc}\left(\frac{z}{\sqrt{4\alpha t}} + \sqrt{\frac{t}{k\rho c/h^2}}\right) \tag{53}$$

The model calculations were compared to the analytical solution using the following parameters: k = 0.2 W/m-K, ρ = 1000 kg/m^3, c = 1400 J/kg-K, $\dot{q}_e''$ = 25 kW/m^2, h = 20 W/m^2-K, and T_0 = 300 K. A grid spacing of 0.1 mm was used, with a constant timetep of 0.1 s. A region 4 cm in thickness was simulated to approximate semi-infinite behavior over 180 s. A comparison of the exact solution and that calculated numerically is given in Figure 2. It can be seen that there is almost an exact match between the analytical solution and that calculated numerically.

5.2. In-depth radiation absorption: finite thickness solid irradiated at one face and insulated at the other

Consider a constant property inert homogeneous solid of thickness δ. It is exposed to a constant radiative heat flux at z = 0 and insulated at its back face ($z = \delta$). Instead of the radiation being absorbed at the surface, it is attenuated in-depth. Heat losses from the irradiated surface are by convection only to the ambient at temperature T_0. The solid is initially at temperature T_0. The problem may be stated mathematically as:

$$\frac{1}{\alpha}\frac{\partial T(z,t)}{\partial t} = \frac{\partial^2 T(z,t)}{\partial z^2} + \frac{\dot{q}_e''\kappa\exp(-\kappa z)}{k} \quad \text{for } 0 \le z \le \delta \tag{54a}$$

$$\frac{\partial T}{\partial z}\bigg|_{z=\delta} = 0 \tag{54b}$$

$$-k\frac{\partial T}{\partial z}\bigg|_{z=0} = -h\big(T - T_0\big)\big|_{z=0} \tag{54c}$$

$$T\big|_{t=0} = T_0 \tag{54d}$$

The exact solution to this problem (obtained using Green's function) is:

$$T - T_0 = \frac{2\dot{q}_e''\kappa^2}{k}\sum_{m=1}^{\infty}\frac{1}{\lambda_m\left(\kappa^2 + \lambda_m^2\right)}\frac{\cos(\lambda_m\delta) + \frac{\lambda_m}{\kappa}\sin(\lambda_m\delta) - \exp(-\kappa\delta)}{\lambda_m\delta + \frac{1}{2}\sin(2\delta\lambda_m)}\cos\big(\lambda_m(\delta - z)\big)\big(1 - \exp\big(-\alpha\lambda_m^2 t\big)\big) \tag{55a}$$

with eigenvalues given by the relation:

$$\cot(\lambda_m \delta) = \frac{k}{h} \lambda_m \tag{55b}$$

The same properties were used as for the semi-infinite solid, except the thickness of the solid was $\delta = 1$ cm and the absorption coefficient was $\kappa = 1000$ m^{-1}. A comparison of the exact and numerical temperature profiles are given in Figure 3. It can again be seen that there is excellent agreement between the model predictions and the exact solution.

5.3. Freezing: Stefan problem

The classical Stefan problem describes the propagation of a solidification front into a semi-infinite medium initially at temperature T_0 above its melting temperature T_m. At time t=0 the solid's surface (at z = 0) is instantaneously dropped to temperature T_∞ (below its melting temperature). When the solid temperature at a given location is lowered to T_m, it solidifies releasing the latent heat of melting (ΔH_m). A solidification front with position given by $s(t)$ begins to propagate into the solid. This front separates the semi-infinite medium into two separate regions: the solid ($z \le s(t)$) and the melt ($z > s(t)$). The governing equations are:

$$\frac{1}{\alpha_s}\frac{\partial T_s}{\partial t} = \frac{\partial^2 T_s}{\partial z^2} \text{ for } 0 \le z \le s(t) \tag{56a}$$

$$\frac{1}{\alpha_\ell}\frac{\partial T_\ell}{\partial t} = \frac{\partial^2 T_\ell}{\partial z^2} \text{ for } s(t) < z < \infty \tag{56b}$$

with boundary and initial conditions:

$$T_s\big|_{z=0} = T_\infty \tag{56c}$$

$$T_\ell\big|_{z\to\infty} = T_0 \tag{56d}$$

$$T_\ell\big|_{t=0} = T_0 \tag{56d}$$

and interface conditions:

$$T_s\big|_{s(t)} = T_\ell\big|_{s(t)} = T_m \tag{56e}$$

$$k_s \left.\frac{\partial T_s}{\partial z}\right|_{s(t)} - k_\ell \left.\frac{\partial T_\ell}{\partial z}\right|_{s(t)} = \rho \frac{ds}{dt} \tag{56f}$$

The solution to this problem is as follows:

$$s(t) = \lambda\sqrt{4\alpha_s t} \tag{57a}$$

$$T_s(z,t) = T_\infty + \frac{T_m - T_\infty}{\mathrm{erf}(\lambda)}\,\mathrm{erf}\left(\frac{z}{\sqrt{4\alpha_s t}}\right) \tag{57b}$$

$$T_\ell(z,t) = T_0 + \frac{T_m - T_0}{\mathrm{erfc}\left(\lambda\sqrt{\alpha_s/\alpha_\ell}\right)}\,\mathrm{erfc}\left(\frac{z}{\sqrt{4\alpha_\ell t}}\right) \tag{57c}$$

Where λ is an eigenvalues given by:

$$\frac{\exp\left(-\lambda^2\right)}{\mathrm{erf}(\lambda)} - \sqrt{\frac{\alpha_s}{\alpha_\ell}}\,\frac{k_\ell}{k_s}\,\frac{T_0 - T_m}{T_m - T_\infty}\,\frac{\exp\left(-\lambda^2\alpha_s/\alpha_\ell\right)}{\mathrm{erfc}\left(\lambda\sqrt{\alpha_s/\alpha_\ell}\right)} = \frac{\sqrt{\pi}\,\lambda\Delta H_m}{c_s\left(T_m - T_\infty\right)} \tag{57d}$$

A comparison of the exact solution and that calculated numerically is given in Figure 4. The parameters used in the calculation were selected to approximate polypropylene, a common melting thermoplastic: $k_s = k_\ell$ = 0.20 W/m-K, $\rho_s = \rho_\ell$ = 900 kg/m^3, $c_s = c_\ell$ = 1700 J/kg-K, T_m = 433 K, T_0 = 438 K, T_∞ = 428 K, and ΔH_m = 50,000 J/kg. This gives an eigenvalues of λ = 0.2317. In the model $\sigma_m^2 = 0.1$ was used with a grid spacing of 0.05 mm. A comparison of the model calculations and the exact solution is given in Figure 4. It can be seen that there is good agreement between the numerical calculations and the exact solution. The slight discrepancies are because the exact solution assumes a well-defined melting temperature whereas in the model the latent heat of melting is distributed over a narrow temperature range as an apparent specific heat.

5.4. Decomposition kinetics

This section simulates the decomposition kinetics of a two-step reaction involving three species, *e.g.* the conversion of a virgin solid to char followed by the subsequent oxidation of the char to form ash. Consider the following coupled ordinary differential equations and initial conditions:

$$\frac{\mathrm{d}Y_A}{\mathrm{d}t} = -Y_A k_{AB} \;\; ; \;\; Y_A(0) = 1 \tag{58a}$$

$$\frac{\mathrm{d}Y_B}{\mathrm{d}t} = Y_A k_{AB} - Y_B k_{BC} \;\; ; \;\; Y_B(0) = 0 \tag{58b}$$

$$\frac{\mathrm{d}Y_C}{\mathrm{d}t} = Y_B k_{BC} \;\; ; \;\; Y_C(0) = 0 \tag{58c}$$

The solution to this problem is:

$$Y_A(t) = \exp(-k_{AB}t) \tag{59a}$$

$$Y_B(t) = \frac{k_{AB}}{k_{BC} - k_{AB}}\left[\exp(-k_{AB}t) - \exp(-k_{BC}t)\right] \tag{59b}$$

$$Y_C(t) = \frac{k_{AB}\left(1 - \exp(-k_{BC}t)\right) + k_{BC}\left(\exp(-k_{AB}t) - 1\right)}{k_{AB} - k_{BC}} \tag{59c}$$

The exact solution in Equation 59 was compared to that calculated numerically for $k_{AB} = 0.389\,\text{s}^{-1}$ and $k_{BC} = 0.262\,\text{s}^{-1}$. The results are shown in Figure 5. It can be seen that there is excellent agreement between the model calculations and the exact solution.

6. Results – simulation of laboratory experiments

The model described above was used to simulate the effect of atmospheric oxygen concentration on the nonflaming gasification of a noncharring solid (PMMA) as well as the thermal pyrolysis of a charring material (white pine). It was also used to simulate the decomposition of an intumescent coating and the propagation of a smolder wave in polyurethane foam.

For simplicity, in these simulations all of the gases were assigned the same properties. The viscosity was calculated assuming a molecular weight of 58 g/mol, a collision diameter of 5.341 Å, and a value of ε/k of 313 K. The specific heat was assumed constant (independent of temperature) and equal to 1000 J/kg-K. Additionally, the first term on the LHS of Eq. 47 was not explicitly calculated because its effect is accounted for by the $\Delta H_{j,k}$ in Eq. 46. All condensed-phase species were assumed to have a permeability of 1×10^{-10} m^2. The initial grid spacing was 0.1 mm (except in the intumescent coating simulation where 0.025 mm was used) and the timestep was constant at 0.1 s. Unless otherwise noted, the back face was impermeable to mass transfer and perfectly insulated. The front face boundary condition is a convective-radiative balance, except for the smoldering simulation where there is no radiation and heat losses are by convection to the ambient.

6.1. Noncharring gasification - PMMA

PMMA decomposition kinetics and thermodynamics (as well as the composition of the volatiles generated) are sensitive to oxygen concentration. This has been demonstrated by Kashiwagi and Ohlemiller [18] by measuring the mass loss rate of PMMA irradiated (under nonflaming conditions) at 17 and 40 kW/m^2 in atmospheres ranging from pure nitrogen to 40% oxygen by volume. It was found that the mass flux rate increases with the oxygen content of the atmosphere, but the oxygen sensitivity is more noticeable at 17 kW/m^2 irradiance than 40 kW/m^2. They hypothesize that this may be because the oxygen concentration in the vicinity of the sample surface is reduced as the mass loss rate increases due to "blowing" from the sample surface. Since the mass loss rates are higher at 40 kW/m^2 irradiance, the surface is better protected by blowing and it is more difficult for oxygen to penetrate into the polymer.

Thes experiments of Kashiwagi and Ohlemiller [18] have been modeled previously by Esfahani and co workers [19, 20]. They related to PMMA decomposition kinetics to the freestream

oxygen concentration, but we take a different approach here by actually modeling the penetration of ambient oxygen into the bubble layer and its resultant effect on the gasification rate. This makes it possible to account for the effects of blowing.

Two condensed-phase species were considered: PMMA and BPMMA. The latter is "bubbled" PMMA having a lower density than the virgin PMMA and a nonzero porosity, thereby allowing oxygen to diffuse from the ambient into the condensed-phase. Four gaseous species are tracked: thermal pyrolysate, oxygen, nitrogen, and oxidative pyrolysate. Three reactions were considered: a condensed-phase to condensed-phase reaction that transforms PMMA to BPMMA, a thermal pyrolysis reaction that transforms BPMMA to thermal pyrolysate in the absence of oxygen, and an oxidative reaction that transforms BPMMA to oxidative pyrolysate while consuming oxygen in the process. For these simulations, there was no melting ($\Delta H_m = 0$), and radiative heat transfer across pores was not modeled ($\gamma = 0$). Properties were estimated with the genetic algorithm described elsewhere [12] for the experiments of Kashiwagi and Ohlemiller [18] at an irradiance of 40 kW/m^2. The parameters used in the simulations are listed in Tables 1 through 4. Note that Table 3 is the matrix $y_{j,k}$ appearing in Equations 43 and 44, and Table 4 is the matrix $\Delta H_{j,k}$ appearing in Equations 45 and 46.

The experimental data and model predictions are shown separately at all oxygen concentrations in Figure 6, and comparisons of the model predictions and experimental data at individual oxygen concentrations are shown in Figure 7. It can be seen that there is very good agreement between the model predictions and the experimental data. The model correctly predicts the trend of a decreasing surface temperature with an increase of oxygen concentration that is observed experimentally. The experimental and predicted mass loss rates match well, but the initial mass loss rate is underpredicted.

Since the parameters were optimized at a heat flux of 40 kW/m^2, the experiments of Kashiwagi and Ohlemiller [18] at 17 kW/m^2 irradiance were used as a "blind" test. The experimental results (at all oxygen levels) are shown in Figure 8a, and the model predictions are shown in Figure 8b. Detailed comparisons are shown in Figures 9a-9d. It can be seen that the model correctly captures the experimentally observed increase in the oxygen sensitivity at 17 kW/m^2 irradiance compared to 40 kW/m^2. The model predicts the surface temperature quite well, but that the mass loss rate is generally underpredicted. This is not surprising since Figure 7 shows that the initial mass loss rate was also underpredicted at 40 kW/m^2 irradianc,. It is likely that better agreement would be obtained with a lower activation energy and pre-exponential factor for the decomposition reactions.

As mentioned earlier, the set of experiments that was simulated here has been modeled by Esfahani and co workers [19, 20] with very good results. However, the effect of oxygen on the decomposition process was incorporated essentially by introducing a pre-exponential factor that varies with the freestream oxygen concentration. Thus, the diffusion of oxygen into the bubble layer was not modeled, so the protective effect of blowing was not captured as it is in the present model. This may explain why different pre-exponential factors and heats of pyrolysis were used in the first paper [19] (where only the experiments at 17 kW/m^2 were simulated) than in the second paper (where only the experiments at 40 kW/m^2 were simulated). In the present work, the model parameters do not depend on heat flux or oxygen concentration.

6.2. Charring gasification – white pine

Ohlemiller, Kashiwagi, and Werner [21, 22] experimentally studied the effects of ambient oxygen concentration on the nonflaming gasification of irradiated white pine. Ref. [22] contains mass loss rate measurements at multiple heat flux levels and oxygen concentrations as well as surface and in-depth thermocouple temperature measurements so it is used here to evaluate the predictive capabilities of the model. In the experiments, white pine cubes 3.8 cm on edge were irradiated at 25 kW/m^2 and 40 kW/m^2 in oxygen concentrations of 0% (pure nitrogen), 10.5%, and 21 % (normal air). The initial density was approximately 380 kg/m^3, with an initial moisture content of approximately 5% by mass.

Although the model has the capability to simulate heat releasing char oxidation reactions, the complexities associated with simulating char oxidation (which becomes important in oxidative environments) are is avoided here by simulating only the experiments conducted under nitrogen. This is done because the primary goal of this section is to demonstrate the generality of the present model, rather than simulate the experiments in detail, and also because oxidative heat releasing reactions are considered later for the simulation of smoldering in polyurethane foam. In the white pine simulations, three condensed-phase species are considered: wet wood, dry wood, and char. Four gaseous species were considered: thermal pyrolysate, nitrogen, oxygen, and water vapor. Both oxygen and nitrogen are essentially passive scalars since they are neither generated nor consumed by reactions. A simple two step reaction mechanism was used. One reaction converts wet wood to dry wood with the release of water vapor (after Atreya [23]). The second reaction is the anaerobic pyrolysis of the dry wood to form char. The model parameters, estimated by genetic algorithm optimization (or assumed) are listed in Tables 5 through 8.

A comparison of the experimental measurements and the model predictions is given in Figures 10 and 11. The model predictions are compared to the experimentally measured [22] mass loss rates in Figure 10 for both 25 kW/m^2 and 40 kW/m^2 irradiance. There is fair agreement between the predicted and measured mass loss rates, although the mass loss rates are overpredicted after the initial peak. The initial mass loss is mostly water vapor, and a reduction in the mass loss rate due to drying is responsible for the "dip" seen in the predicted mass loss rate curve, a feature not observed experimentally. A comparison of the experimentally measured [22] and modeled temperatures at several depths below the surface is shown in Figure 11 for an irradiance of 40 kW/m^2 (nitrogen atmosphere). There is excellent agreement between the predicted and measured temperatures.

The experiments of Kashiwagi, Ohlemiller, and Werner [22] have been simulated by Jia *et al.* [24] and Weng *et al.* [25] using integral charring models. As was done here, Jia *et al.* [24] modeled the only the experiments [22] that were conducted in pure nitrogen because their model did not include exothermic char oxidation. Weng *et al.* [25] recently modeled the experiments [22] with a previously-developed integral model that was modified to explicitly consider char oxidation. Both groups obtained good agreement between the model predictions and the experimental data. However, the agreement between the temperature predictions of the present model and the experimental data [22] is considerably better than in the study of Jia *et al.* [24],

probably because here temperature-dependent thermal properties were used and the input parameters were purposely optimized with the genetic algorithm.

6.3. Intumescent coating

Griffin *et al.* [26] studied the effect of atmospheric oxygen concentration on intumescent coatings using thermogravimetry, differential thermal analysis, and cone calorimetry. As a test of the model, we selected their "material A", an epoxy-based coating with an inorganic filler consisting of glass/silica fibers. The experiments simulated include thermogravimetric tests conducted in a nitrogen atmosphere (heating rates of 10, 15, 20, and 30 ºC/min) and Cone Calorimeter tests conducted at an irradiance of 90 kW/m^2 in a "reduced O_2" atmosphere having an oxygen concentration between 8% and 10%.

In this set of simulations, the effect of oxygen on the decomposition reactions is not explicitly modeled, so the gaseous species conservation equation (Equation 19) and the pressure evolution equation (Equation 22) are not solved. Instead, the pyrolysate mass flux inside is calculated from the equation for conservation of gas-phase mass, Equation 20. Five condensed-phase species are considered: virgin1, virgin2, char, intumesce, and ash. Two reactions that result in mass loss are considered: the first converts species virgin1 (having an initial mass fraction of 0.91) to char, and the second converts char to ash. A third reaction is considered that converts virgin2 (having an initial mass fraction of 0.09) to a low-density "intumesce" without any release of gases. It is this reaction that causes the swelling of the intumescent coating.

As with the other simulations, the genetic algorithm optimization procedure described elsewhere [12, 13] was used to estimate the model parameters. These parameters are summarized in Tables 9 through 12. The density of the coating was unknown, so it was estimated (somewhat arbitrarily) at 1,000 kg/m^3. A comparison of the experimental differential thermogravimetric curves and those predicted with the model are shown in Figure 12. It can be seen that the model captures the main features of the curves, but not all of the details. However, this is to be expected since only two reactions that result in mass loss are considered. Figure 13 gives a comparison of the modeled and experimentally measured substrate temperature and coating thickness. The surface temperature is substantially overpredicted, but there is good agreement between the measured and predicted transient thickness of the coating (due to intumescence, the thickness increases by a factor of almost 20). Some of the difference between the measured and predicted temperature of the substrate temperature may be attributed to inaccurate specification of the initial density (which was unknown) or the back-face boundary conditions. It was difficult to estimate the contact resistance between the coating and the substrate and the back-face boundary condition of the substrate, all of which affect the substrate temperature.

6.4. Smolder – polyurethane foam

The final experiment modeled in this paper is the smoldering of polyurethane foam in microgravity, with the experimental data originally reported by Bar-Ilan *et al.* [27]. The experiments involve the smoldering of polyurethane cylinder 12 cm in diameter and 14 cm in length and were conducted in microgravity on the NASA Space Shuttle. It was ignited at one end by a constant heat flux that resulted in a nominally linear increase of the temperature at the

igniter (centerline thermocouple temperatures were recorded at eight axial locations, including the igniter). Air was forced into the foam sample at the igniter end so that the smolder propagation was in the same direction as the airflow (forward smolder). While the igniter was energized (during the first 400 s of the experiment), the forced airflow velocity was approximately 0.01 mm/s. The igniter was de-energized at 400 s, at which point the airflow was increased to its nominal value. Two experiments were conducted having nominal forced airflow velocities of 3 mm/s and 5 mm/s.

This smolder experiment has already been simulated with a model designed specifically to simulate smoldering by Rein *et al.* [28]. Although their model is formulated differently than the present model, we adopt their basic modeling approach. Specifically, only two condensed-phase species are considered: virgin foam and char. Two reactions are considered: an anaerobic thermal pyrolysis reaction that converts virgin foam to char, and a foam oxidation reaction that converts foam to char while consuming oxygen and releasing heat. The gaseous species that are tracked include thermal pyrolysate, nitrogen, oxygen, and oxidative pyrolysate. The model parameters, determined by genetic algorithm optimization, are listed in Tables 13 - 16.

In the simulations, the temperature at the igniter was specified for the first 400 s. After that, heat losses were by convection to the ambient, assuming a heat transfer coefficient of 0.3 W/m^2-K. To account for radial heat losses, a volumetric heat transfer coefficient of 14 W/m^3-K was used, approximately three times greater than that used by Rein *et al.* [28]. Figure 14 shows the calculated temperature profiles as a function of time for the 3 mm/s airflow case. Figure 15a gives a comparison of the model predictions and the experimental temperature data for the 3 mm/s airflow case, and Figure 15b gives the comparison for the 5 mm/s airflow case. In the 3 mm/s airflow case, the smolder wave propagates at a steady rate of approximately 0.2 mm/s and eventually reaches the end of the foam sample. Rein *et al.* [28] calculated a lower propagation velocity of 0.1 mm/s and found that the smolder reaction was quenched, as occurred in the experiments. Here, the quenching of the smolder reaction is not predicted, but this could be attributed to differences in heat losses or reaction enthalpies. The calculated smolder velocity for the 5 mm/s airflow case was 0.3 mm/s, compared with approximately 0.26 mm/s calculated by Rein *et al.* [28]. The solution bifurcation reported by Rein *et al.* [28] at 5 mm/s airflow velocity was not observed here. Similar to Rein *et al.* [28], the peak temperatures are well-predicted for the 3 mm/s case, but underpredicted for the 5 mm/s case. This may be due to the neglect of char oxidation in the present model.

7. Concluding remarks

This paper presents the formulation of a generalized pyrolysis model. Its flexibility is demonstrated by simulating four experiments: thermo-oxidative decomposition of a noncharring solid, thermal pyrolysis of a charring solid, gasification and swelling of an intumescent coating, and smoldering in a porous medium. Good agreement between the model predictions and the experimental data was observed, particularly considering that the model was not developed specifically to simulate a particular material or class of materials.

The ultimate goal of pyrolysis modeling (at least in the fire field) is the prediction of large-scale fire behavior through combined gaseous and condensed phase modeling. One of the biggest

barriers to reaching this goal is the difficulty associated with characterizing practical materials in terms of the parameters needed by pyrolysis models. Here, we estimated the required input parameters using a previously developed genetic algorithm [12, 13] which locates a set of model input parameters that provides optimal agreement between model predictions and experimental data (from bench scale fire tests, thermogravimetry, etc.). However, there are few experimental measurements reported in the fire literature which are suitable for extracting all of the required model input parameters. This is largely because modern bench-scale fire tests measure a material's overall reaction to fire and provide a means to estimate effective flammability properties (thermal inertia, ignition temperature, etc.), but they are not intended as a means to estimate the parameters needed for numerical pyrolysis modeling. Consequently, development of a customized fire test (or modifications to an existing fire test) that is designed specifically to provide the required input parameters would make the task of property estimation for pyrolysis modeling much less difficult.

Acknowledgments

This work was supported by NASA Glenn Research Center under Grant NNC-05GA02G. The first author would also like to thank NASA for support under the Graduate Student Researcher Program, Grant NNC-04HA08H, sponsored by NASA Glenn Research Center. The authors would like to thank G.J. Griffin for providing the experimental data for the intumescent coating in spreadsheet form. Many discussions critical to the model development process were held with Jose Torero and Guillermo Rein, and we would like to thank them for their insight and suggestions.

References

1. Di Blasi, C., "Modeling and Simulation of Combustion Processes of Charring and Non-Charring Solid Fuels," *Progress in Energy and Combustion Science* **19** 71-104 (1993).
2. Kashiwagi, T., "Polymer Combustion and Flammability-Role of the Condensed Phase," *Proceedings of the Combustion Institute* **25** 1423-1437 (1994).
3. Fernandez-Pello, A.C., "The Solid Phase," In *Combustion Fundamentals of Fire*, Ed. G. Cox, cademic Press, New York, pp. 31-100, 1995.
4. Di Blasi C., "The state of the art of transport models for charring solid degradation," *Polymer International* **49** 1133-1146 (2000).
5. Lyon, R.E. & Janssens, M.L., "Polymer Flammability," DOT/FAA/AR-05/14, 2005.
6. Moghtaderi, B., "The State-of-the-Art in Pyrolysis Modeling of Lignocellulosic Solid Fuels," *Fire and Materials* **30** 1-34 (2006).
7. Lautenberger, C. & Fernandez-Pello, A.C., "Pyrolysis Modeling, Thermal Decomposition, and Transport Processes in Combustible Solids," to appear in *Transport Phenomena in Fires*, Ed. M. Faghri & B. Sunden, WIT Press, 2006.
8. Staggs, J.E.J., "Modeling Thermal Degradation of Polymers Using Single-Step First-Order Kinetics," *Fire Safety Journal* **32** 17-34 (1999).
9. Kuo, J.T. & Hsi, C.-L., "Pyrolysis and Ignition of Single Wooden Spheres Heated in High-Temperature Streams of Air," *Combustion and Flame* **142** 401-412 (2005).

10. Di Blasi, C., "Modeling the Effects of High Radiative Heat Fluxes on Intumescent Material Decomposition," *Journal of Analytical and Applied Pyrolysis* **71** 721-737 (2004).
11. Leach, S.V., Rein, G., Ellzey, J.L. & Ezekoye, O.A., "Kinetic and Fuel Property Effects on Forward Smoldering Combustion," *Combustion and Flame* **120** 346-358 (2000).
12. Lautenberger, C., Rein, G. & Fernandez-Pello, A.C., "The Application of a Genetic Algorithm to Estimate Material Properties for Fire Modeling from Bench-Scale Fire Test Data," *Fire Safety Journal* **41** 204-214 (2006).
13. Rein, G., Lautenberger, C., Fernandez-Pello, A.C., Torero, J.L. & Urban, D.L., "Application of Genetic Algorithms and Thermogravimetry to Determine the Kinetics of Polyurethane Foam in Smoldering Combustion," *Combustion and Flame* **146** 95-108 (2006).
14. McGrattan, K., Fire Dynamics Simulator (Version 4) Technical Reference Guide, NIST Special Publication 1018, 2004.
15. Lautenberger, C., McAllister, S., Rich, D., and Fernandez-Pello, C., "Modeling the Effect of Environmental Variables on Opposed-flow Flame Spread Rates with FDS," Fire Safety in Tall Buildings International Congress, University of Cantabria, Santander Spain, October 18-20 2006.
16. Bird, R.B., Stewart, W.E., & Lightfoot, E.N., *Transport Phenomena*, John Wiley & Sons, New York, 1960.
17. Patankar, S.V., *Numerical Heat Transfer and Fluid Flow*, Hemisphere Publishing Corporation, New York, 1980.
18. Kashiwagi, T. & Ohlemiller, T.J., "A Study of Oxygen Effects on Nonflaming Transient Gasification of PMMA and PE during Thermal Irradiation," *Proceedings of the Combustion Institute* **19** 815-823 (1982).
19. Esfahani, J.A., "Oxygen-Sensitive Thermal Degradation of PMMA: a Numerical Study," *Combustion Science and Technology* **174** 183-198 (2002).
20. Esfahani, J.A., Ayani, M.B., & Shirin, M.B., "A transient two-dimensional model of thermal and oxidative degradation of PMMA," *Iranian Journal of Science & Technology, Transaction B, Engineering* **29 B2** 207-218 (2005).
21. Ohlemiller, T.J., Kashiwagi, T., & Werner, K., "Wood Gasification at Fire Level Heat Fluxes," *Combustion and Flame* **69** 155-170 (1987).
22. Kashiwagi, T., Ohlemiller, T.J., & Werner, K., "Effects of External Radiant Flux and Ambient Oxygen Concentration on Nonflaming Gasification Rates and Evolved Products of White Pine," *Combustion and Flame* **69** 331-345 (1987).
23. Atreya, A., "Ignition of Fires," *Philosophical Transactions of the Royal Society A: Mathematical, Physical, and Engineering Sciences* **356** 2787-2813 (1998).
24. Jia, F., Galea, E.R., & Patel, M.K., "Numerical Simulation of the Mass Loss Process in Pyrolyzing Char Materials," *Fire and Materials* **23** 71-78 (1999).
25. Weng, W.G., Hasemi, Y., and Fan, W.C., "Predicting the pyrolysis of wood considering char oxidation under different ambient oxygen concentrations," *Combustion and Flame* **145** 723-729 (2006).
26. Griffin, G.J., Bicknell, A.D., & Brown, T.J., "Studies on the Effect of Atmospheric Oxygen Content on the Thermal Resistance of Intumescent, Fire-Retardant Coatings," *Journal of Fire Sciences* **23** 303-328 (2005).

27. Bar-Ilan, A., Rein, G., Fernandez-Pello, A.C., Torero, J.L., & Urban, D.L., "Forced forward smoldering experiments in microgravity," *Experimental Thermal and Fluid Science* **28** 743-751 (2004).
28. Rein, G., Bar-Ilan, A., Fernandez-Pello, A.C., Ellzey, J.L., Torero, J.L., & Urban, D.L., "Modeling of one-dimensional smoldering of polyurethane in microgravity conditions," *Proceedings of the Combustion Institute* **30** 2327-2334 (2005).

List of figures

Figure 1. Control volume system.
Figure 2. Comparison of exact solution and numerical model prediction for semi-infinite solid with surface absorption of radiation and surface heat losses by convection.
Figure 3. Comparison of exact solution and numerical model prediction for finite thickness irradiated solid with in-depth radiation absorption and surface heat losses by convection.
Figure 4. Comparison of exact solution and model prediction for Stefan problem.
Figure 5. Comparison of exact solution and numerical model prediction for coupled ordinary differential equations.
Figure 6. Surface temperature and mass loss rate of PMMA irradiated at 40 kW/m^2.
Figure 7. Comparison of experimental [18] and modeled surface temperature and mass loss rates of PMMA irradiated at 40 kW/m^2.
Figure 8. Surface temperature and mass loss rate of PMMA irradiated at 17 kW/m^2.
Figure 9. Comparison of experimental [18] and modeled surface temperature and mass loss rates of PMMA irradiated at 17 kW/m^2.
Figure 10. Comparison of experimentally measured [22] and modeled mass loss rate of white pine in nitrogen atmosphere.
Figure 11. Comparison of experimentally measured [22] and modeled temperatures at several depths below the surface of white pine irradiated at 40 kW/m^2 in nitrogen atmosphere.
Figure 12. Comparison of experimentally measured [26] and modeled differential thermogravimetric curves of an intumescent coating (material A from Ref. [26]) in nitrogen atmosphere at several heating rates.
Figure 13. Comparison of experimentally measured [26] and modeled substrate temperature and thickness an intumescent coating (material A from Ref. [26]) irradiated at 90 kW/m^2 in the Cone Calorimeter (reduced O_2 atmosphere).
Figure 14. Calculated temperature profiles in smoldering polyurethane foam as a function of time.
Figure 15. Comparison of experimentally measured [27] and modeled temperature at several locations in a polyurethane foam cylinder smoldering in microgravity. a) 3 mm/s airflow velocity; b) 5 mm/s airflow velocity

List of tables

Table 1. Condensed-phase parameters for PMMA simulations.
Table 2. Reaction parameters for PMMA simulations.
Table 3. Gaseous yields for PMMA simulations.
Table 4. Gaseous heats of reaction (J/kg) for PMMA simulations.
Table 5. Condensed-phase parameters for white pine simulations.
Table 6. Reaction parameters for white pine simulations.
Table 7. Gaseous yields for white pine simulations.
Table 8. Gaseous heats of reaction (J/kg) for white pine simulations.
Table 9. Condensed-phase parameters for intumescent coating simulations.
Table 10. Reaction parameters for intumescent coatings simulations.
Table 11. Gaseous yields for intumescent coating simulations.
Table 12. Gaseous heats of reaction (J/kg) for intumescent coating simulations.
Table 13. Condensed-phase parameters for smolder simulations.
Table 14. Reaction parameters for smolder simulations.
Table 15. Gaseous yields for smolder simulations.
Table 16. Gaseous heats of reaction (J/kg) for smolder simulations.

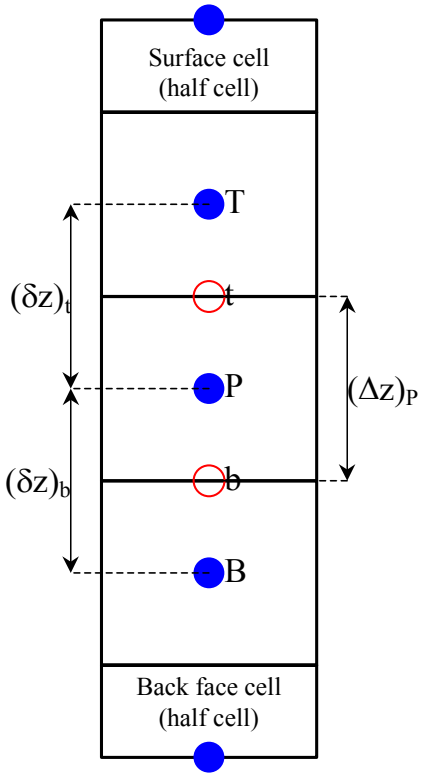

Figure 1. Control volume system.

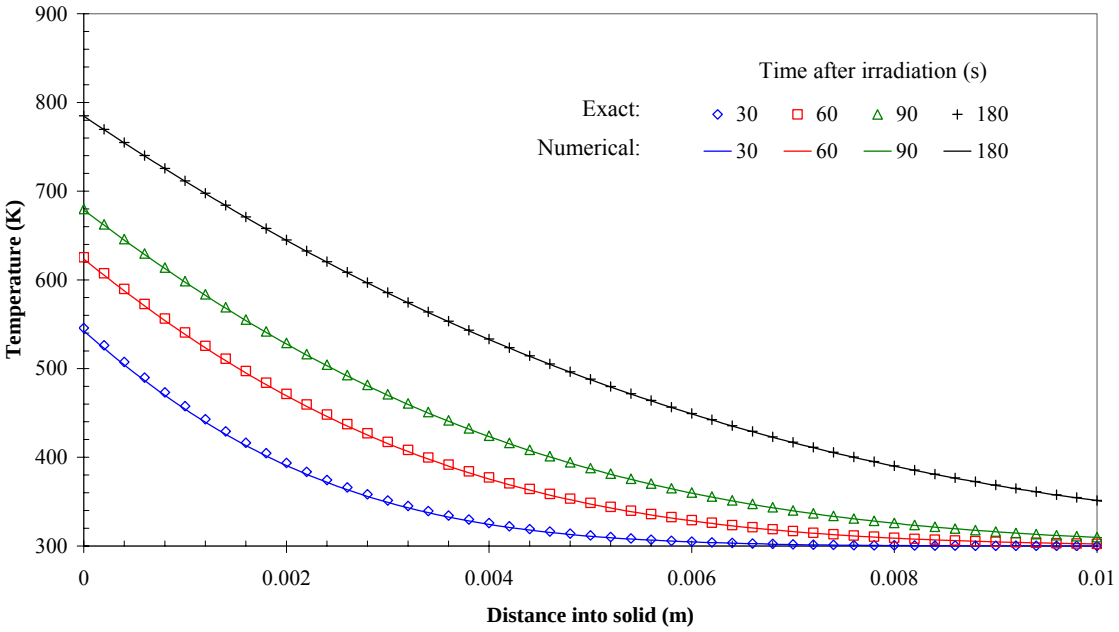

Figure 2. Comparison of exact solution and numerical model prediction for semi-infinite solid with surface absorption of radiation and surface heat losses by convection.

Figure 2

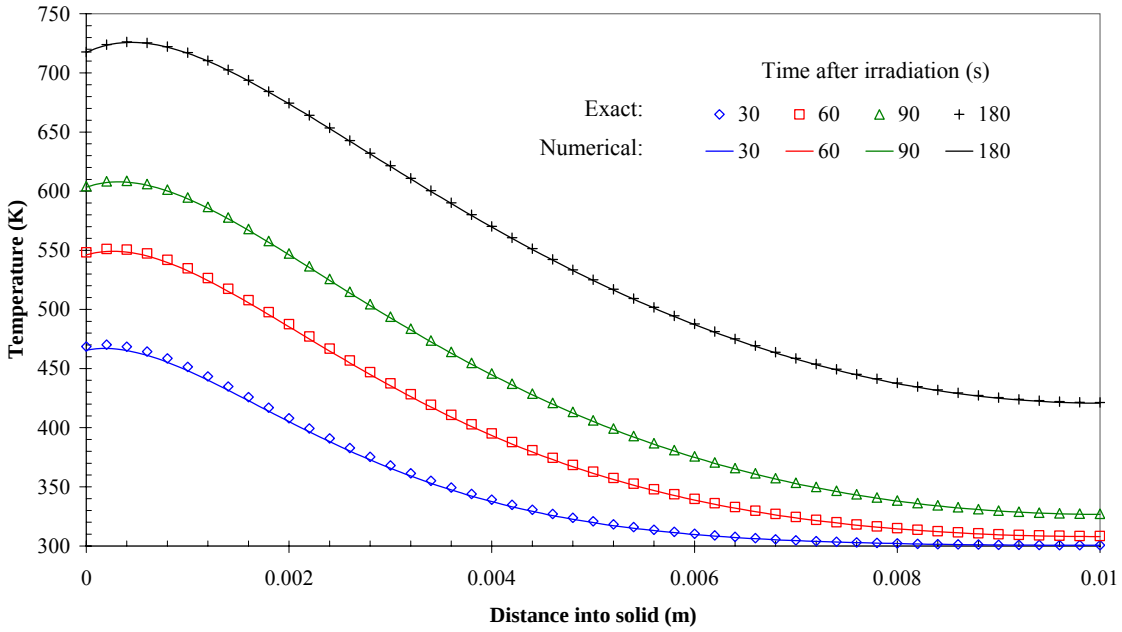

Figure 3. Comparison of exact solution and numerical model prediction for finite thickness irradiated solid with in-depth radiation absorption and surface heat losses by convection.

Figure 3

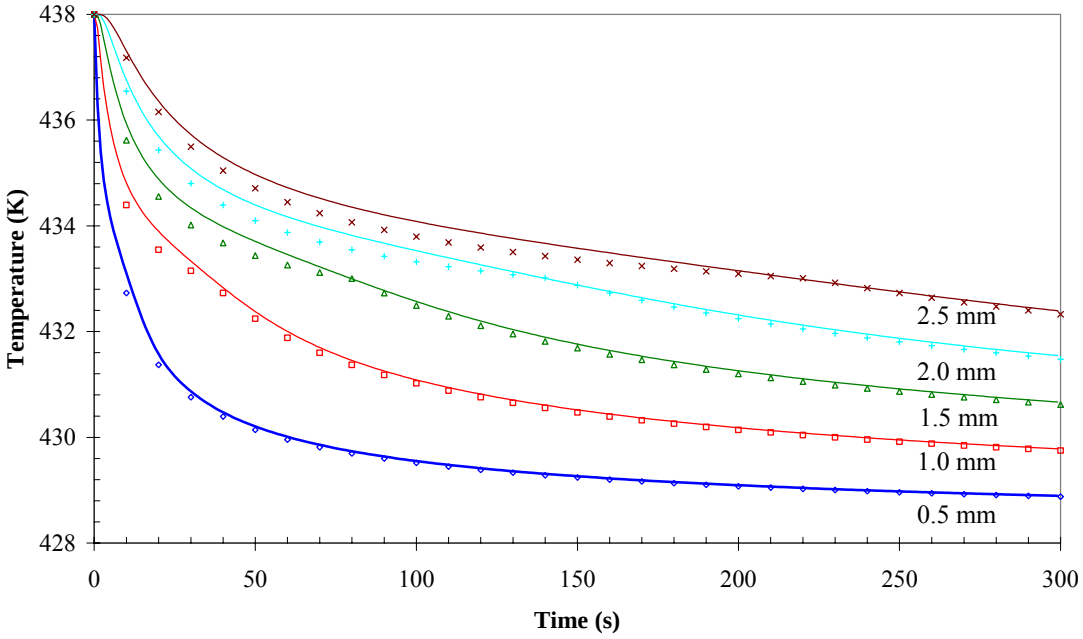

Figure 4. Comparison of exact solution and model prediction for Stefan problem. Solid lines are model prediction and individual points are exact solution. Distance from front face is indicated in plot.

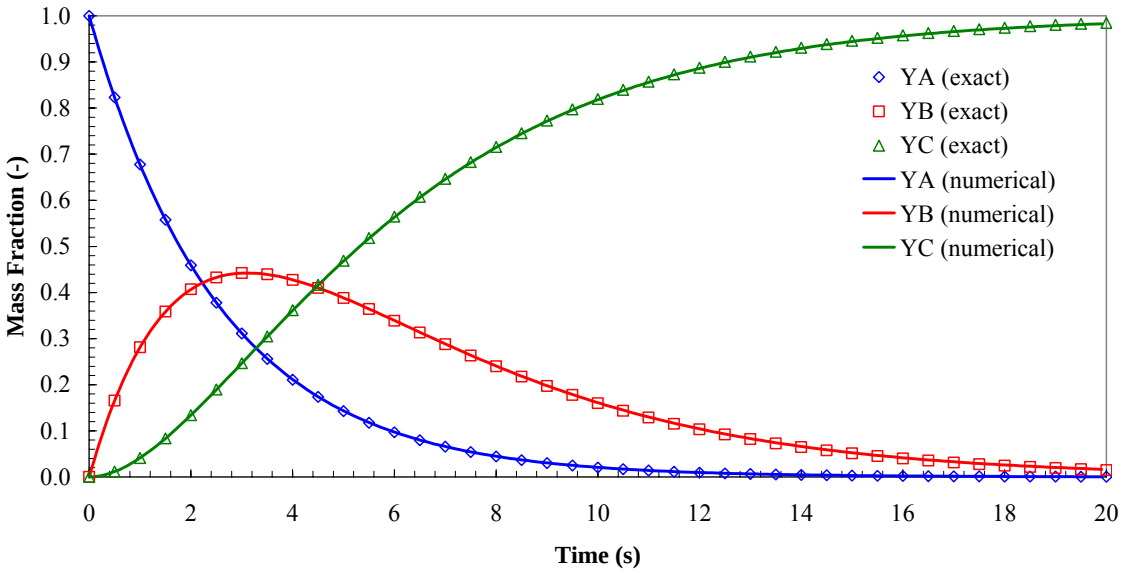

Figure 5. Comparison of exact solution and numerical model prediction for coupled ordinary differential equations.

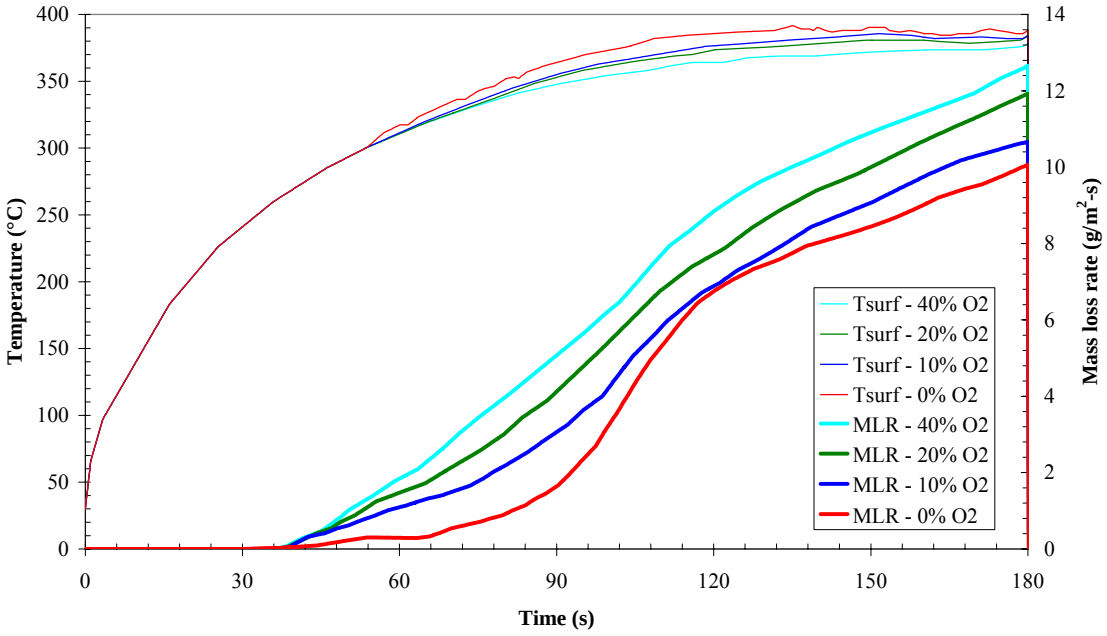

(a)

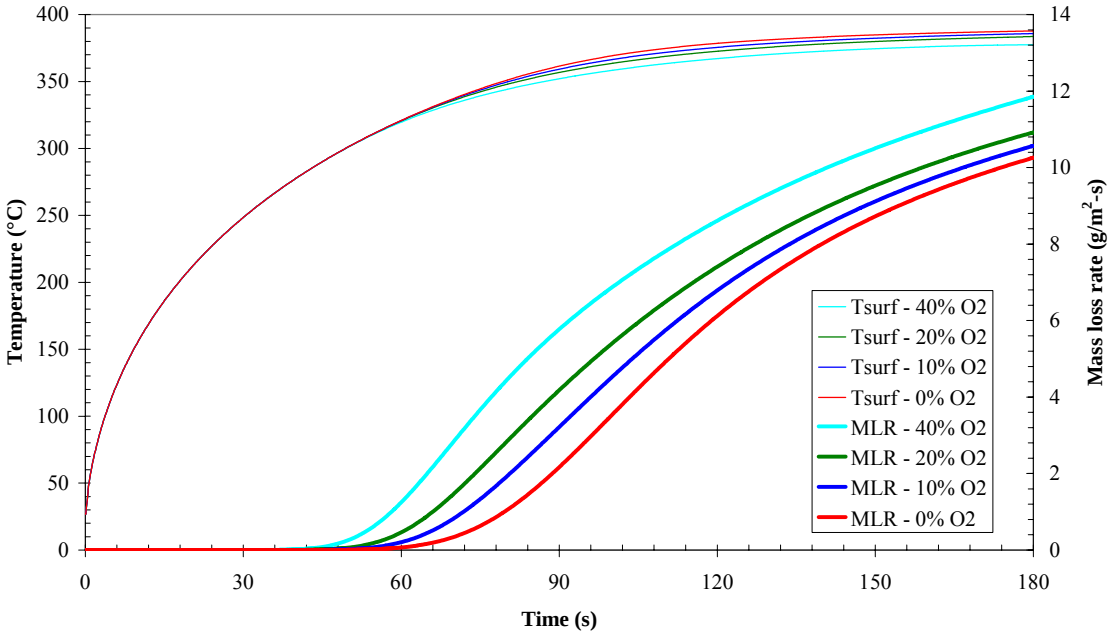

(b)

Figure 6. Surface temperature and mass loss rate of PMMA irradiated at 40 kW/m^2. a) Experimental data [18]; b) Model.

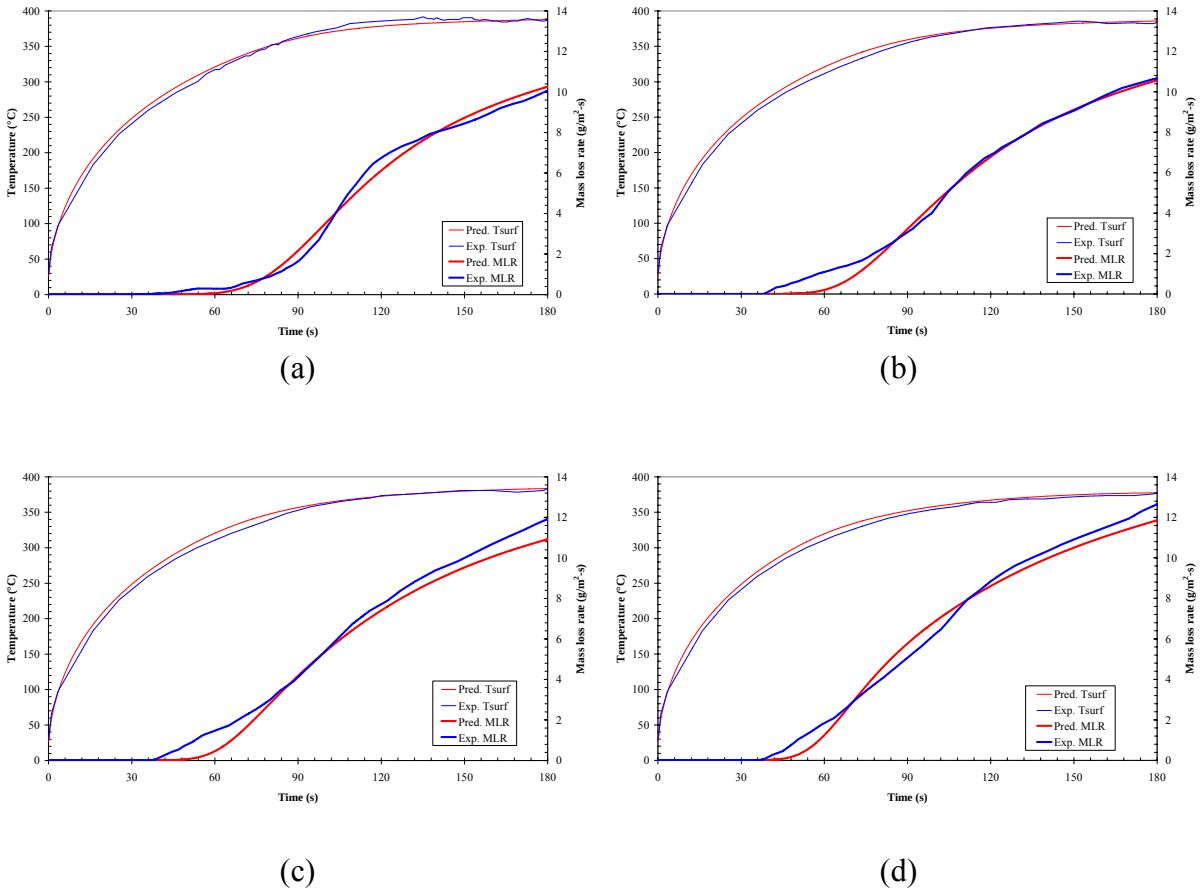

Figure 7. Comparison of experimental [18] and modeled surface temperature and mass loss rates of PMMA irradiated at 40 kW/m^2.
a) nitrogen atmosphere; b) 10% O_2 atmosphere; c) 20% O_2 atmosphere; 40% O_2 atmosphere.

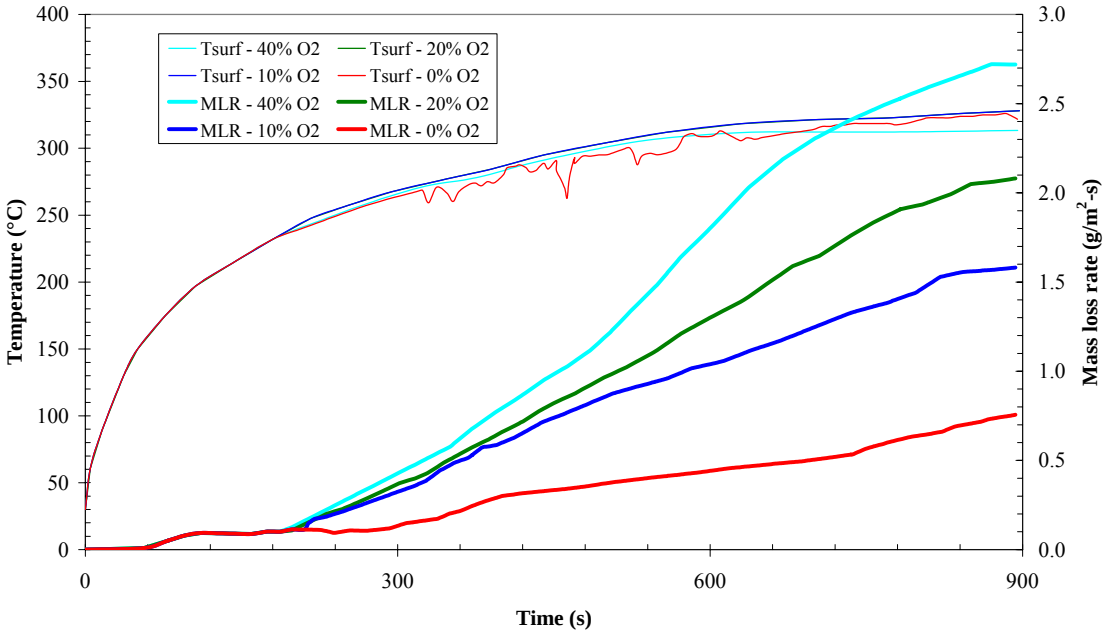

(a)

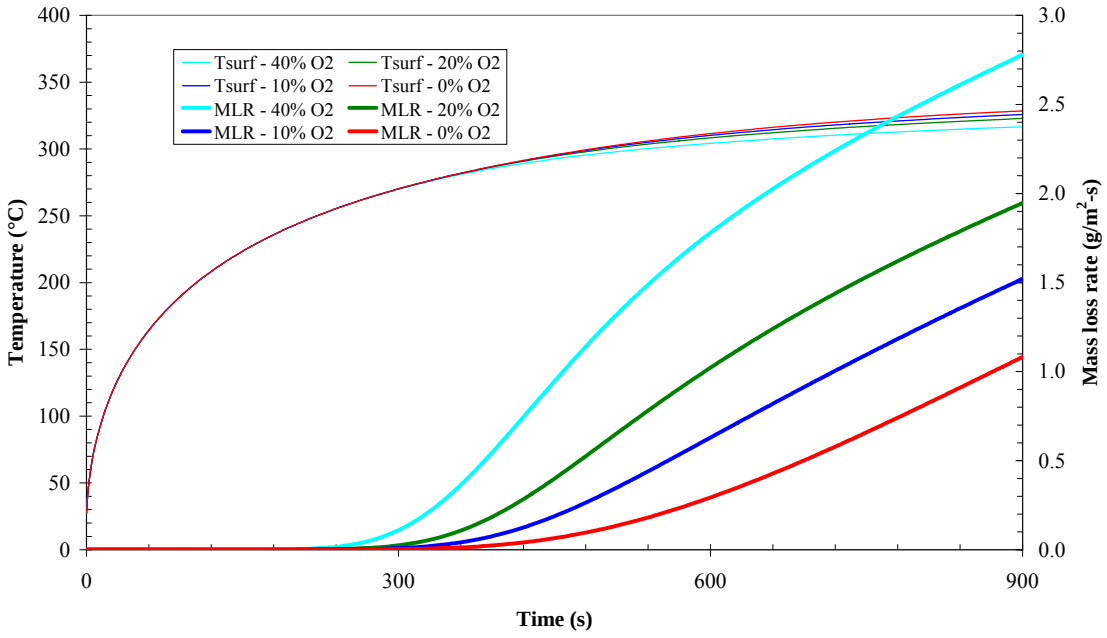

(b)

Figure 8. Surface temperature and mass loss rate of PMMA irradiated at 17 kW/m^2. a) Experimental data [18]; b) Model.

Figure 8

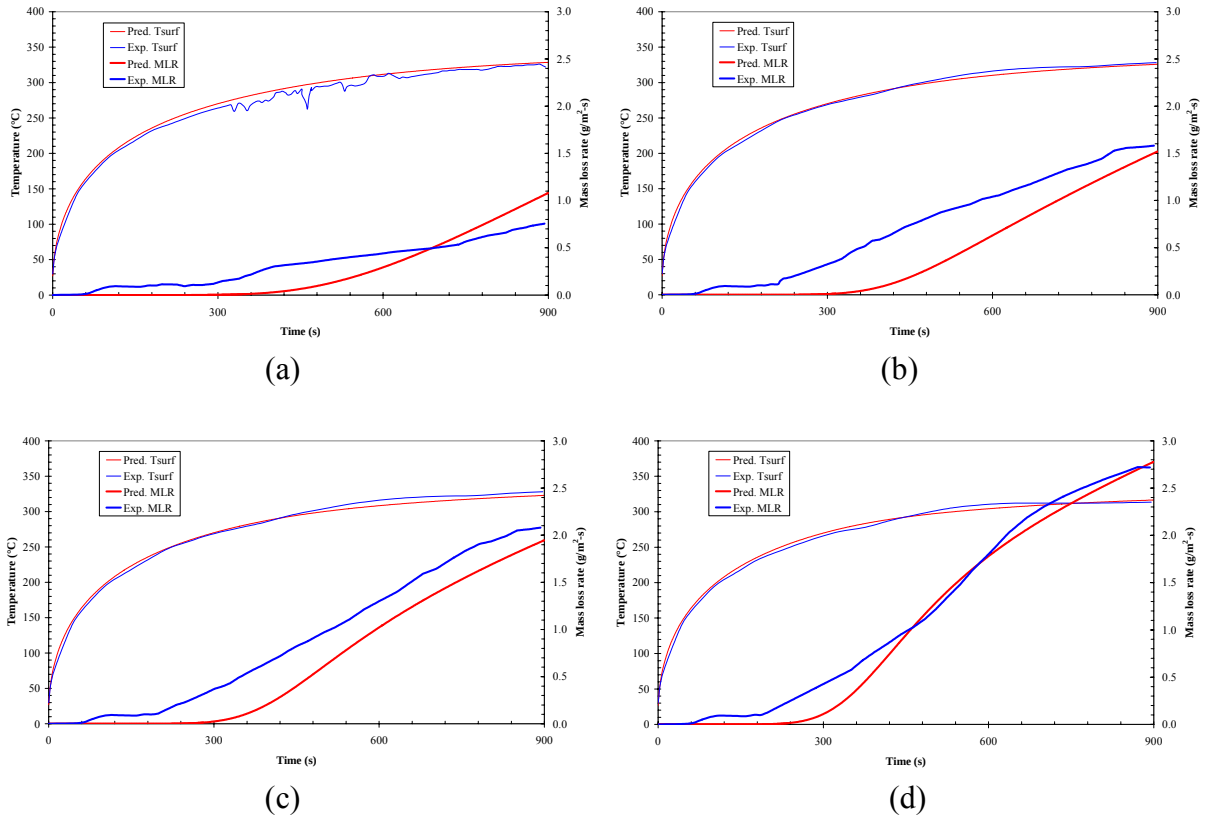

Figure 9. Comparison of experimental [18] and modeled surface temperature and mass loss rates of PMMA irradiated at 17 kW/m^2.
a) nitrogen atmosphere; b) 10% O_2 atmosphere; c) 20% O_2 atmosphere; 40% O_2 atmosphere.

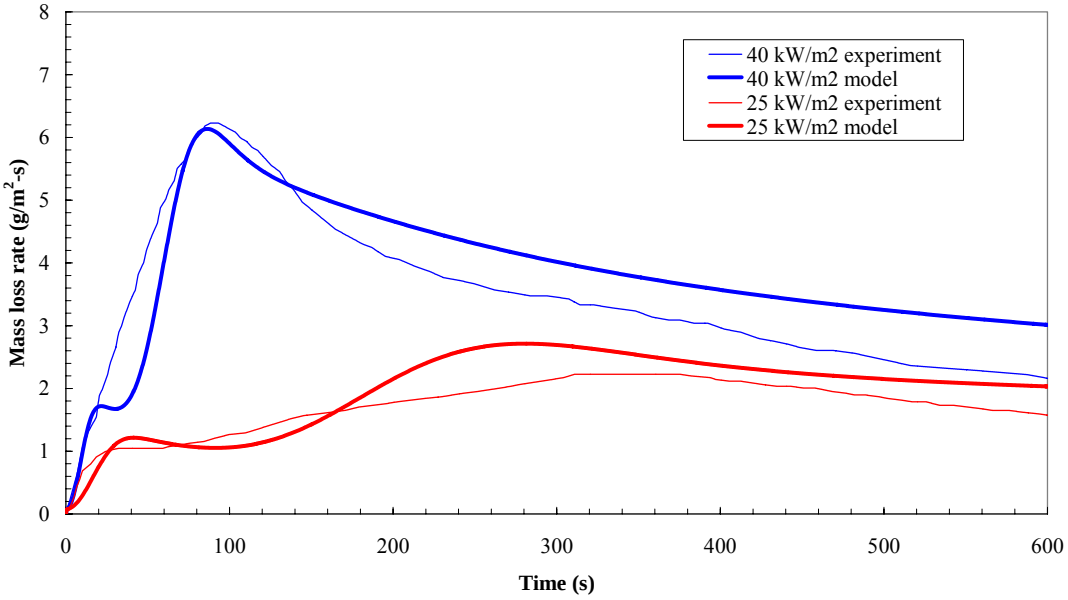

Figure 10. Comparison of experimentally measured [22] and modeled mass loss rate of white pine in nitrogen atmosphere.

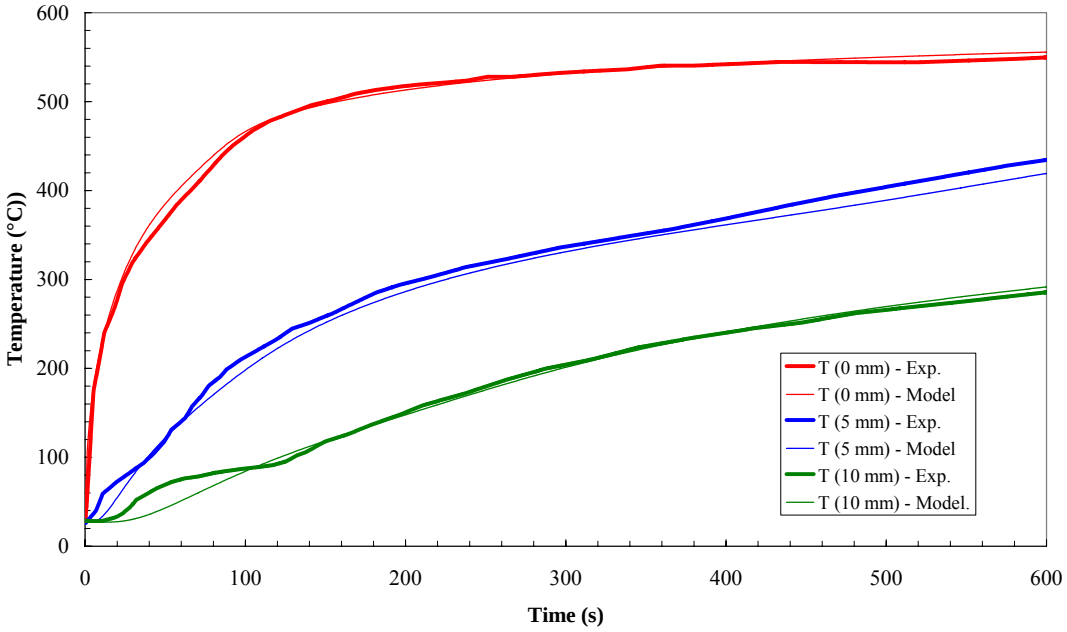

Figure 11. Comparison of experimentally measured [22] and modeled temperatures at several depths below the surface of white pine irradiated at 40 kW/m^2 in nitrogen atmosphere.

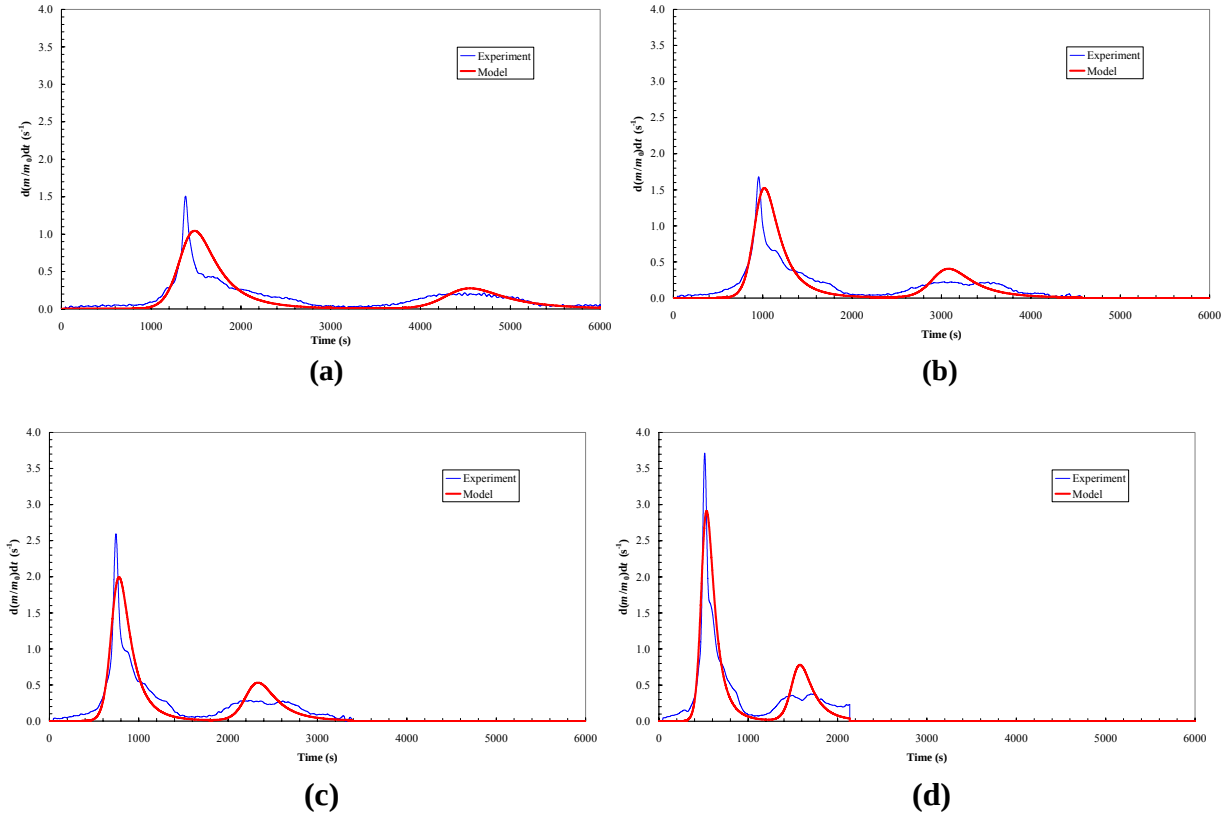

Figure 12. Comparison of experimentally measured [26] and modeled differential thermogravimetric curves of an intumescent coating (material A from Ref. [26]) in nitrogen atmosphere at several heating rates.
a) 10 ºC/min; b) 15 ºC/min; c) 20 ºC/min; d) 30 ºC/min;

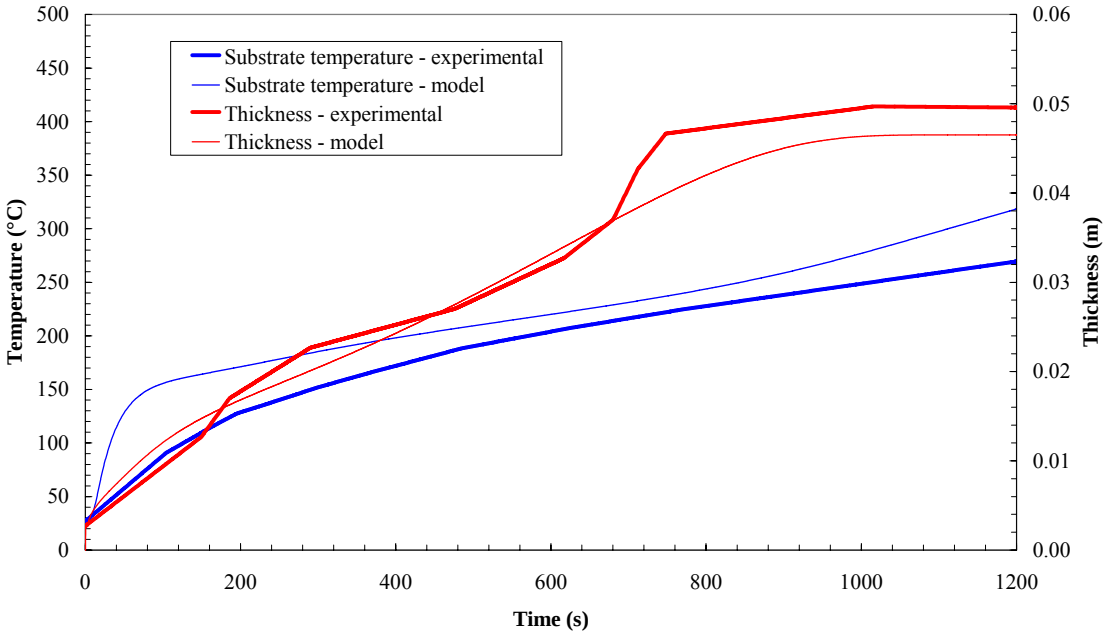

Figure 13. Comparison of experimentally measured [26] and modeled substrate temperature and thickness an intumescent coating (material A from Ref. [26]) irradiated at 90 kW/m^2 in the Cone Calorimeter (reduced O_2 atmosphere).

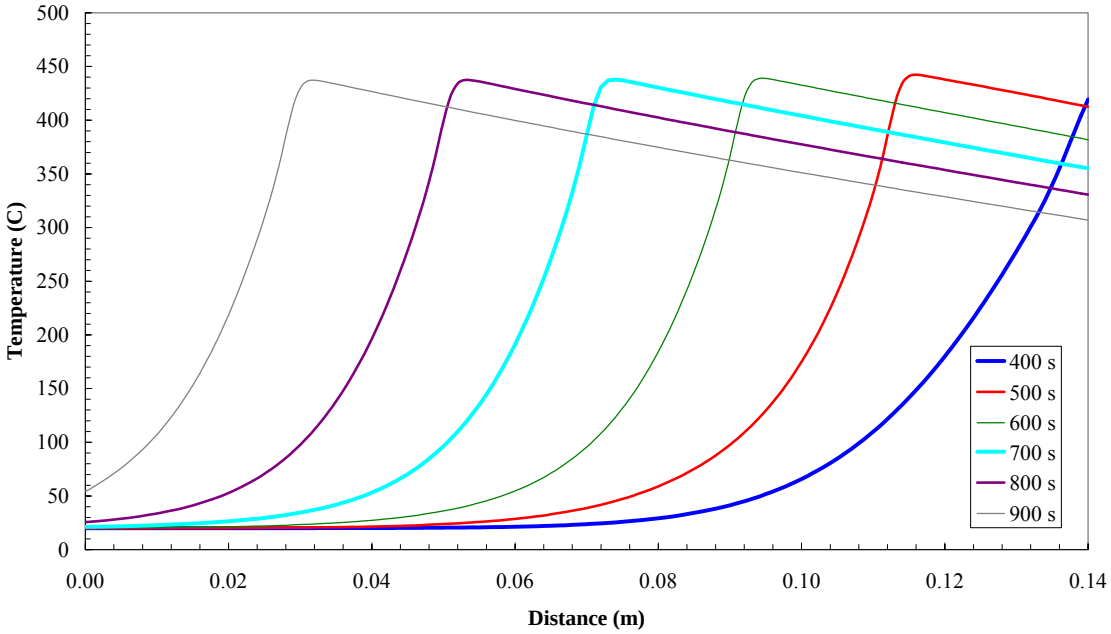

Figure 14. Calculated temperature profiles in smoldering polyurethane foam as a function of time.

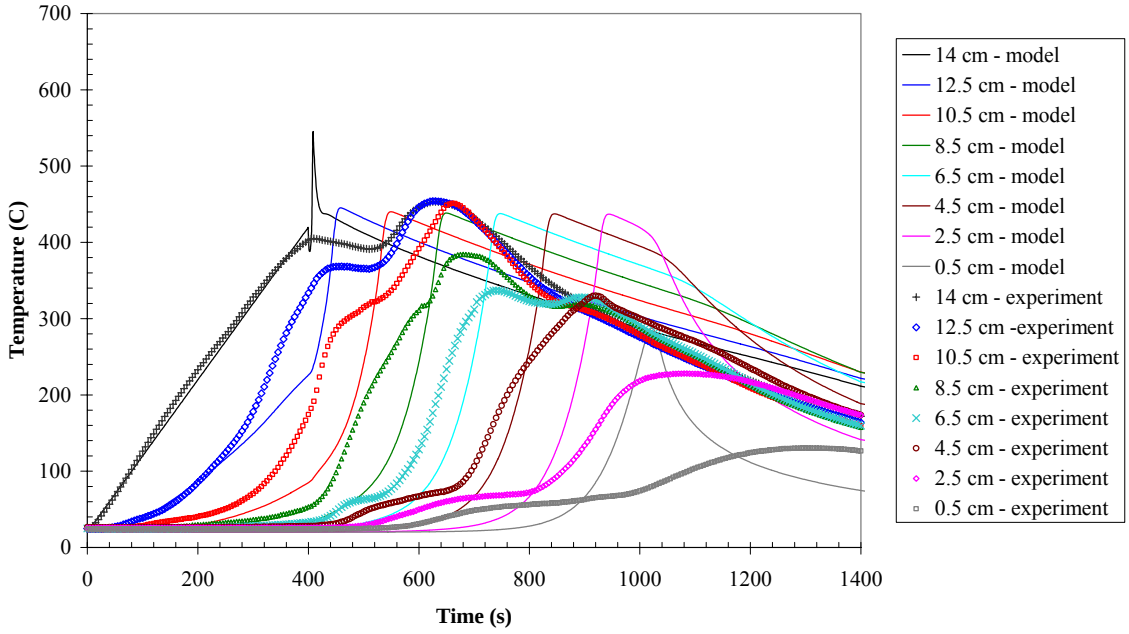

(a)

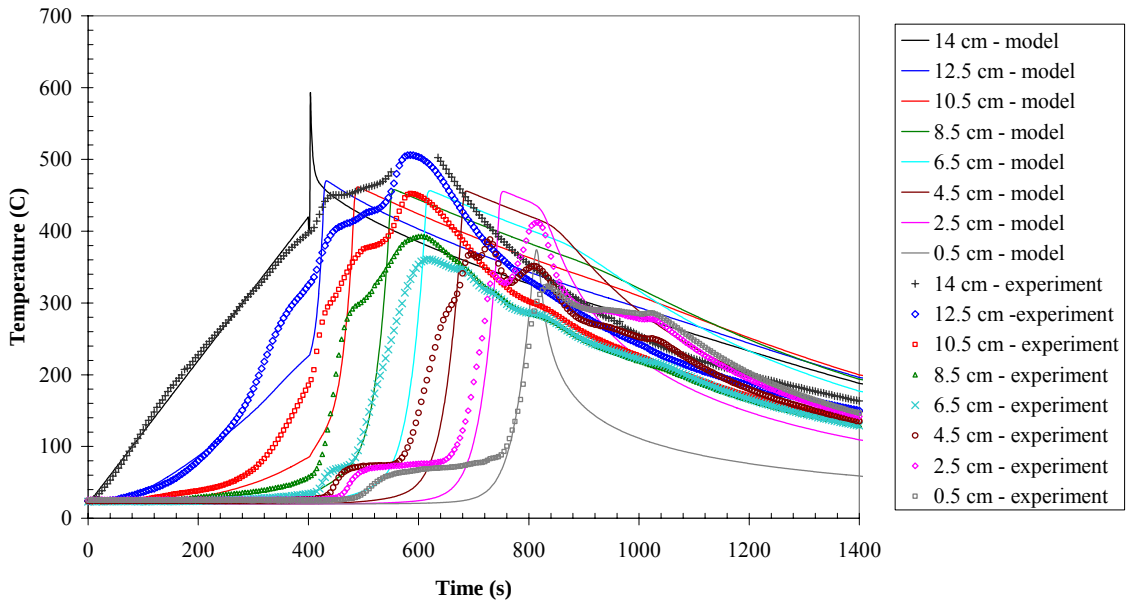

(b)

Figure 15. Comparison of experimentally measured [27] and modeled temperature at several locations in a polyurethane foam cylinder smoldering in microgravity. a) 3 mm/s airflow velocity; b) 5 mm/s airflow velocity

Table 1. Condensed-phase parameters for PMMA simulations.

i	Name	k_0 (W/m-K)	n_k (–)	ρ_0 (kg/m^3)	n_ρ (–)	c_0 (J/kg-K)	n_c (–)	ε (–)	κ (m^{-1})	ψ (m^3/m^3)
1	PMMA	0.22	0.20	1190	-0.1	2060	0.47	0.92	4200	5×10^{-5}
2	BPMMA	0.22	0.20	1134	-0.1	2070	0.47	0.92	3990	0.05

Table 2. Reaction parameters for PMMA simulations.

k	From	To	χ (–)	ΔH (J/kg)	A (s^{-1})	E (kJ/mol)	n (-)	n_{O2} (-)
1	PMMA	BPMMA	1	0	1.41×10^{11}	141.1	1.32	0
2	BPMMA	GASES	1	0	5.58×10^{11}	170.0	1.10	0
3	BPMMA	GASES	1	0	5.58×10^{11}	170.0	1.10	11.9

Table 3. Gaseous yields for PMMA simulations.

j \ *k*	1	2	3
1 (thermal pyrolysate)	0	1.00	0
2 (oxygen)	0	0	-0.10
3 (nitrogen)	0	0	0
4 (oxidative pyrolysate)	0	0	1.10

Table 4. Gaseous heats of reaction (J/kg) for PMMA simulations.

j \ *k*	1	2	3
1 (thermal pyrolysate)	0	-5.37×10^5	0
2 (oxygen)	0	0	0
3 (nitrogen)	0	0	0
4 (oxidative pyrolysate)	0	0	-3.03×10^5

Table 5. Condensed-phase parameters for white pine simulations.

i	Name	k_0 (W/m-K)	n_k (–)	ρ_0 (kg/m^3)	n_ρ (–)	c_0 (J/kg-K)	n_c (–)	ε (–)	κ (m^{-1})	ψ (m^3/m^3)
1	wet pine	0.29	0.39	380	0	2500	0.13	0.90	∞	0.001
2	dry pine	0.24	0.37	361	0	2480	0.13	0.90	∞	0.05
3	char	0.21	0.35	69	0	2290	0.12	0.95	∞	0.82

Table 6. Reaction parameters for white pine simulations.

k	From	To	χ (–)	ΔH (J/kg)	A (s^{-1})	E (kJ/mol)	n (-)	n_{O2} (-)
1	wet wood	dry wood	1	0	4.50×10^{3}	44.0	1	0
2	dry wood	char	1	0	1.82×10^{11}	163.6	1.79	0

Table 7. Gaseous yields for white pine simulations.

j \ *k*	1	2
1 (thermal pyrolysate)	0	1
2 (nitrogen)	0	0
3 (water vapor)	1	0
4 (oxygen)	0	0

Table 8. Gaseous heats of reaction (J/kg) for white pine simulations.

j \ *k*	1	2
1 (thermal pyrolysate)	0	-2.56×10^5
2 (nitrogen)	0	0
3 (water vapor)	-2.40×10^6	0
4 (oxygen)	0	0

Table 9. Condensed-phase parameters for intumescent coating simulations.

i	Name	k_0 (W/m-K)	n_k (–)	ρ_0 (kg/m^3)	n_ρ (–)	c_0 (J/kg-K)	n_c (–)	ε (–)	κ (m^{-1})	ψ (m^3/m^3)
1	virgin1	0.14	0	1000	0	1730	0	1	∞	NA
2	virgin2	0.19	0	1000	0	2460	0	1	∞	NA
3	char	0.04	0	320	0	1870	0	1	∞	NA
4	intumesce	0.08	0	6	0	2360	0	1	∞	NA
5	ash	0.02	0	35	0	2150	0	1	∞	NA

Table 10. Reaction parameters for intumescent coatings simulations.

k	From	To	χ (–)	ΔH (J/kg)	A (s^{-1})	E (kJ/mol)	n (-)	n_{O2} (-)
1	virgin1	char	1	0	4.31×10^{10}	133.5	3.38	0
2	virgin2	intumesce	0	0	4.22×10^{10}	130.9	0.91	0
3	char	ash	1	0	2.14×10^{13}	316.4	3.36	0

Table 11. Gaseous yields for intumescent coating simulations.

j \ *k*	1	2	3
1	1	1	1

Table 12. Gaseous heats of reaction (J/kg) for intumescent coating simulations.

j \ *k*	1	2	3
1	-1.92×10^4	-2.06×10^5	-3.57×10^5

Table 13. Condensed-phase parameters for smolder simulations.

i	Name	k_0 (W/m-K)	n_k (–)	ρ_0 (kg/m^3)	n_ρ (–)	c_0 (J/kg-K)	n_c (–)	ε (–)	κ (m^{-1})	ψ (m^3/m^3)
1	foam	0.06	0.4	26.5	0	1700	0	NA	NA	0.97
2	char	0.06	0.4	10.6	0	1700	0	NA	NA	0.99

Table 14. Reaction parameters for smolder simulations.

k	From	To	χ (–)	ΔH (J/kg)	A (s^{-1})	E (kJ/mol)	n (-)	n_{O2} (-)
1	foam	char	1	0	5.0×10^{15}	200	3	0
2	foam	char	1	0	6.0×10^{11}	155	1	1

Table 15. Gaseous yields for smolder simulations.

j \ *k*	1	2
1 (thermal pyrolysate)	1	0
2 (nitrogen)	0	0
3 (oxygen)	0	-0.4
4 (oxidative pyrolysate)	0	1.4

Table 16. Gaseous heats of reaction (J/kg) for smolder simulations.

j \ *k*	1	2
1 (thermal pyrolysate)	-7.75×10^5	0
2 (nitrogen)	0	0
3 (oxygen)	0	-1.31×10^6
4 (oxidative pyrolysate)	0	1